2010

Subhorizontal fabric in exhumed continental lower crust and implications for lower crustal flow: Athabasca granulite terrane, western Canadian Shield

Gregory Dumond
University of Massachusetts Amherst

Philippe Goncalves
Université de Franche-Comté

Michael L. Williams
University of Massachusetts Amherst

Michael J. Jercinovic
University of Massachusetts Amherst

Recommended Citation

Dumond, Gregory; Goncalves, Philippe; Williams, Michael L.; and Jercinovic, Michael J., "Subhorizontal fabric in exhumed continental lower crust and implications for lower crustal flow: Athabasca granulite terrane, western Canadian Shield" (2010). *Tectonics*. 33.
https://doi.org/10.1029/2009TC002514

Subhorizontal fabric in exhumed continental lower crust and implications for lower crustal flow: Athabasca granulite terrane, western Canadian Shield

Gregory Dumond,[1,2] Philippe Goncalves,[3] Michael L. Williams,[1] and Michael J. Jercinovic[1]

Received 2 April 2009; accepted 28 October 2009; published 25 March 2010.

[1] The >20,000 km^2 Athabasca granulite terrane is one of Earth's largest exposures of continental lower crust. The terrane is underlain by heterogeneous isobarically cooled orthogneisses termed the Mary batholith. A transect across the batholith documents early, penetrative subhorizontal to gently dipping gneissic foliation (S_1). Kilometer- to meter-scale domains of S_1 contain lineations (L_1) defined by ribbons of recrystallized K-feldspar + plagioclase + quartz + amphibole ± orthopyroxene. L_1 coincides with garnet aggregates, elongate mafic enclaves, and core-and-mantle structure in feldspar porphyroclasts. Lineations are coaxial with hinges of isoclinally folded layering (F_1). L_1 is interpreted as a composite mineral lineation with intersection and stretching components. Kinematics are uniformly top-to-the-ESE. Thermobarometry derived from synkinematic phases is compatible with granulite-grade (~800°C) ductile lower crustal flow during D_1 at ~0.9 GPa (~30 km paleodepths). Results from electron probe microanalyzer (EPMA) Th-U-total Pb monazite geochronology support Neoarchean (circa 2.60–2.55 Ga) garnet growth and melt-enhanced flow. Metamorphic reactions accompanying D_1 strain were synkinematic, with preferential nucleation of high-Ca garnet and amphibole in the Na-rich mantles of recrystallized plagioclase porphyroclasts. Relatively H_2O-poor and/or CO_2-rich conditions during D_1 are required by the preservation of fine-grained microstructures. Subhorizontal tectonites in the Mary batholith may represent an important field-based analog for lower crustal flow during orogenesis or large magnitude extension. The results illustrate the evolving strength of continental lower crust. Neoarchean subhorizontal flow of weak lower crust was followed by near-isobaric cooling and strengthening. Paleoproterozoic deformation events produced steep fabrics (S_2), steeply dipping shear zones, and reactivation of S_1, a record of strain localization and strain hardening in an isobarically cooled anisotropic medium. **Citation:** Dumond, G., P. Goncalves, M. L. Williams, and M. J. Jercinovic (2010), Subhorizontal fabric in exhumed continental lower crust and implications for lower crustal flow: Athabasca granulite terrane, western Canadian Shield, *Tectonics*, *29*, TC2006, doi:10.1029/2009TC002514.

1. Introduction

[2] Flow of continental lower crust is inferred to exert a primary control on surface topography and potentially leads to extensive lateral redistribution of mass and heat in collisional orogens, e.g., the Himalayan-Tibetan system [*Beaumont et al.*, 2004]. Continental lower crustal flow during orogenesis requires the formation of a rheologically weak lower crust that may flow in response to lateral pressure gradients produced by topographic loads or crustal thickening [*Royden*, 1996; *Royden et al.*, 1997, 2008]. Crustal flow is characterized by the development of penetrative gently dipping fabrics produced by high-temperature deformation mechanisms [*Rutter and Brodie*, 1992]. These pervasive, gently dipping ductile fabrics represent one plausible explanation for the characteristically high reflectivity and lamellae observed in the lower crustal portions of many deep seismic reflection profiles [e.g., *Meissner et al.*, 2006]. These dramatic reflection patterns have been documented across numerous collisional orogens, including: the Pyrenees, the Himalayas, and the Trans-Hudson [*Hajnal et al.*, 2005; *Hauck et al.*, 1998; *Ross et al.*, 2004; *Roure et al.*, 1989]. A fundamental issue in all of the above observations concerns the deformation mechanisms that attend lower crustal flow and the degree to which lower crust partitions strain [e.g., *Williams and Jiang*, 2005; *Williams et al.*, 2006]. Field studies of exposed continental lower crust are required for constraining geophysical results and testing thermal-mechanical models, which necessarily oversimplify an inherently heterogeneous and anisotropic medium. With rare exceptions, there remain few well-documented field examples of rocks that record the effects of lower crustal flow at >25–30 km paleodepths, e.g., the Central Gneiss Belt of the western Grenville Province, Canada [see *Culshaw et al.*, 1997].

[1]Department of Geosciences, University of Massachusetts, Amherst, Massachusetts, USA.
[2]Now at Department of Earth, Atmospheric, and Planetary Sciences, Massachusetts Institute of Technology, Cambridge, Massachusetts, USA.
[3]UMR 6249 Chrono-Envrionnement, Université de Franche-Comté, Besançon, France.

0278-7407/10/2009TC002514

[3] Field-based studies aimed at understanding fabric development in continental lower crust are motivated by three fundamental issues. First, geophysical transects and coupled thermal-mechanical models provide strong evidence for low-viscosity flow of continental lower crust during collisional orogenesis [*Beaumont et al.*, 2004; *Haines et al.*, 2003; *Jamieson et al.*, 2004; *Ozacar and Zandt*, 2004; *Ross et al.*, 2004]. Field-based data provide a basis for interpreting geophysical results and a more robust framework for developing numerical models that adequately describe the evolution of continental lower crust in orogenic systems with respect to deformation, metamorphism, magmatism, and erosion [e.g., *Jamieson et al.*, 2007]. Second, the mechanisms of subhorizontal fabric development in continental lower crust remain controversial [e.g., *Meissner et al.*, 2006; *Sandiford*, 1989]. Two end-member models include prograde deformation during crustal thickening [*Park*, 1981], or extension due to orogenic collapse and/or lithospheric delamination [*Sandiford and Powell*, 1986]. Field-based examples of subhorizontal fabric in continental lower crust provide a means for evaluating these models. Finally, penetrative deformation of continental crust due to any plate tectonic-scale process requires failure of the entire thickness of continental lithosphere [*Kusznir and Park*, 1986]. The inference that continental lower crust is weak (i.e., relative to the upper crust and mantle) has been used to explain the presence of distributed low-viscosity deformation at lower crustal levels across laterally extensive regions like the Tibetan plateau [*Bird*, 1991; *Gratton*, 1989; *Hodges*, 2006; *Klemperer*, 2006; *Royden et al.*, 1997; *Westaway*, 1995], strike-slip plate boundaries like the Alpine fault zone of New Zealand [*Wilson et al.*, 2004], and regions of large-magnitude extension like the Basin and Range of western North America [*Kruse et al.*, 1991; *Wernicke et al.*, 2008]. These inferences are commonly deduced remotely from surface observations. The study of deformation and metamorphism in exposed continental lower crust, preserving subhorizontal fabrics not extensively overprinted by later tectonic events, permits interpretations of lower crustal rheology based on direct observations of lower crustal fabric [e.g., *Handy and Zingg*, 1991].

[4] In this contribution, we present new structural, thermobarometric, and geochronological results from a high-resolution, across-strike transect of an exhumed exposure of continental lower crust in northern Saskatchewan, Canada (Figures 1 and 2). Thermodynamic modeling and geochronology suggest that prior to the onset of circa 1.9–1.7 Ga uplift and exhumation, at least part of the exposure resided at lower crustal levels for 650 Myr or more [*Flowers et al.*, 2008; *Mahan et al.*, 2008]. This record permits an unprecedented view of the behavior of continental lower crust from Archean assembly to Paleoproterozoic reworking [*Williams and Hanmer*, 2006]. A notable feature of this exposure is a ubiquitous, subhorizontal to gently dipping, early granulite-grade fabric (S_1), variably overprinted by steep fabrics and localized high-strain zones (S_2) (Figures 3 and 4) [see also *Mahan et al.*, 2008]. We hypothesize that the early fabric is a directly observable record of lower crustal flow at ~30–40 km paleodepths. The deep crustal flow is correlated with Neoarchean collisional orogenesis documented elsewhere in the western Churchill cratonic province of the Canadian Shield. Penetrative ductile flow was followed by a period of isobaric cooling and strengthening of the lower crust prior to Paleoproterozoic lithospheric reactivation.

2. Geologic Setting

[5] The western Canadian Shield of North America is underlain by Archean cratonic provinces, including the Slave, Churchill, Sask, and Superior provinces, separated by Paleoproterozoic orogens and shear zones (Figure 1a) [*Ansdell et al.*, 1995; *Hoffman*, 1988; *Whitmeyer and Karlstrom*, 2007]. The western Churchill province is one of the world's largest and least understood regions of cratonic lithosphere [e.g., *Hartlaub et al.*, 2005; *van Breeman et al.*, 2007a]. The Great Slave Lake shear zone and the circa 2.0–1.9 Ga Taltson-Thelon orogen mark the northwestern limit of the western Churchill province [*Hoffman*, 1987; *Ross*, 2002]. The circa 1.9–1.8 Ga Trans-Hudson orogen defines the southeastern boundary (Figure 1a) [*Ansdell*, 2005; *St-Onge et al.*, 2006]. The western Churchill province is subdivided into the Rae and Hearne domains by the Snowbird tectonic zone, a >2800 km long NE trending geophysically defined lineament (Figure 1a) [*Hoffman*, 1988].

[6] The central portion of the Snowbird tectonic zone is well exposed north of the circa 1.7 Ga Athabasca basin in northern Saskatchewan [*Rainbird et al.*, 2007]. The triangular shape of the zone is attributed to the interaction of crosscutting intracontinental thrust and strike-slip shear zones (Figure 1b) [*Mahan and Williams*, 2005]. The western part of the zone is defined by the >400 km long, 5 to 7 km wide Grease River shear zone. Dextral, strike-slip strain and SW-over-NE thrusting occurred along the structure at circa 1.92–1.90 Ga at lower crustal conditions (650–700°C and 0.9–1.0 GPa ≈ 30–40 km paleodepths) [*Dumond et al.*, 2008]. The eastern part of the zone is defined by the >500 km long, 5 to 10 km wide Legs Lake shear zone. The structure accommodated dextral, thrust-sense shearing during uplift of a large exposure of granulite-facies continental lower crust to ~0.5 GPa (~15 km paleodepths) at circa 1.85 Ga [*Mahan et al.*, 2003; *Mahan et al.*, 2006a, 2006b]. Uplift along the Legs Lake shear zone at circa 1.85 Ga occurred synchronous with strike-slip reactivation of the Grease River shear zone during dextral transpression [*Dumond et al.*, 2008]. Last, circa 1.8 Ga brittle-ductile, dextral strike-slip shear zones offset the Legs Lake shear zone at upper crustal levels, including reactivation of the Grease River and Virgin River shear zones (Figure 1b) [*Card*, 2001; *Dumond et al.*, 2008; *Mahan and Williams*, 2005].

2.1. Athabasca Granulite Terrane

[7] The Athabasca granulite terrane consists of > 20,000 km^2 of continental lower crust deformed at 0.8 to >1.5 GPa (~25 to >50 km paleodepths), exposed north of the Athabasca basin (Figure 1b) [*Mahan and Williams*, 2005; *Mahan et al.*, 2008]. The region is underlain by Archean to Paleo-

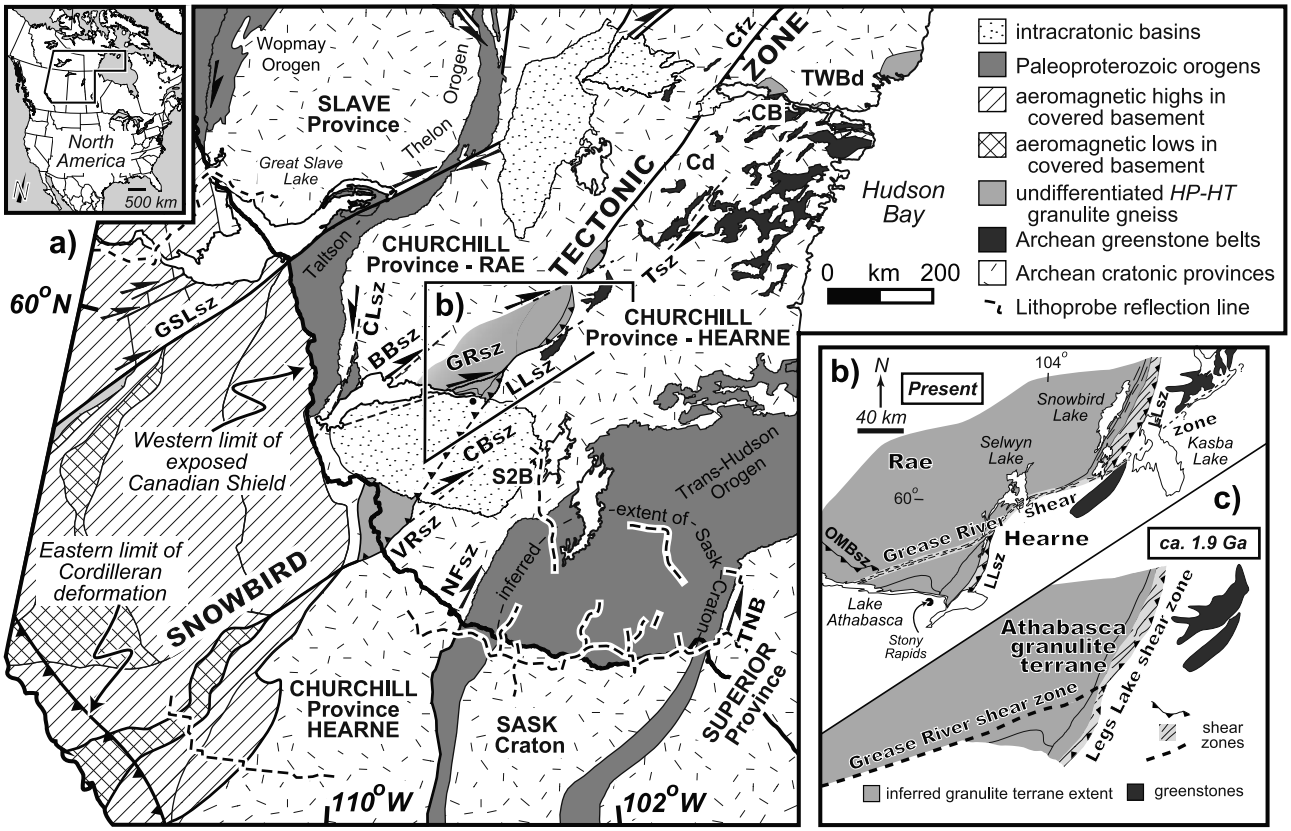

Figure 1. (a) Simplified geologic map of the western Canadian Shield compiled and modified after *Hoffman* [1988], *Tella et al.* [2000], *Ross* [2002], and *Hajnal et al.* [2005]. Note location of Figure 1b at center. Abbreviations are GSLsz, Great Slave Lake shear zone; CLsz, Charles Lake shear zone; BBsz, Black Bay shear zone; GRsz, Grease River shear zone; LLsz, Legs Lake shear zone; CBsz, Cable Bay shear zone; VRsz, Virgin River shear zone; NFsz, Needle Falls shear zone; TNB, Thompson Nickel Belt; Tsz, Tyrell shear zone; Cd, Chesterfield domain; Cfz, Chesterfield fault zone [*Berman et al.*, 2007]; TWBd, Tehery Wager Bay gneiss domain [*van Breeman et al.*, 2007b]. CB, Cross Bay complex [*Hanmer et al.*, 2006]. Locations of Lithoprobe seismic reflection profiles from http://www.lithoprobe.ca. (b) Present-day disposition of Athabasca granulite terrane. Figure 2 illustrates detailed geologic map of Athabasca granulite terrane depicted in Figure 1b. OMBsz, Oldman-Bulyea shear zone [*Card*, 2001]. (c) Circa 1.9 Ga reconstruction of Athabasca granulite terrane after *Mahan and Williams* [2005] (compare to Figure 1b).

proterozoic mafic and felsic granulites, orthogneisses, and minor paragneisses that are cut by the Legs Lake shear zone on the eastern margin of the terrane (Figures 1b and 2) [*Mahan and Williams*, 2005; *Mahan et al.*, 2008; *Martel et al.*, 2008]. The exposure represents continental lower crust of the Rae domain juxtaposed with middle crustal rocks of the Hearne domain via ~20 km of vertical throw along the Legs Lake shear zone [*Mahan et al.*, 2003]. The overall geometry is analogous to other crustal-scale, intracontinental thrust systems like the Kapuskasing uplift of the Superior Province [*Percival and West*, 1994] or the Red Bank thrust of Australia [*Teyssier*, 1985].

[8] Two main generations of structures and fabrics have been identified throughout the terrane. The first generation (D_1) includes subhorizontal to NW striking, moderately dipping gneissic fabrics (S_1) and recumbent isoclinal folds (F_1) of compositional layering (S_0) or a relict tectonic fabric (S_{1-n}). Early fabrics typically have WNW trending stretching and intersection lineations [*Ashton et al.*, 2006; *Mahan and Williams*, 2005; *Martel et al.*, 2008]. The second generation (D_2) includes upright, open to isoclinal F_2 folds of S_1 and local transposition of NW trending folds and gneissic fabrics into subvertical to steeply dipping, NE striking mylonitic foliations (S_2) with shallowly to moderately plunging, NE to SW trending stretching and intersection lineations [*Ashton et al.*, 2006; e.g., *Hanmer et al.*, 1995; *Mahan et al.*, 2003, 2008; *Martel et al.*, 2008]. The timing and possible linkage of these deformation events to two lower crustal granulite-grade events at circa 2.62–2.55 Ga and circa 1.92–1.89 Ga remains the subject of over a decade of ongoing research and debate [*Ashton et al.*, 2007; *Baldwin et al.*, 2003, 2004, 2006, 2007; *Berman et al.*,

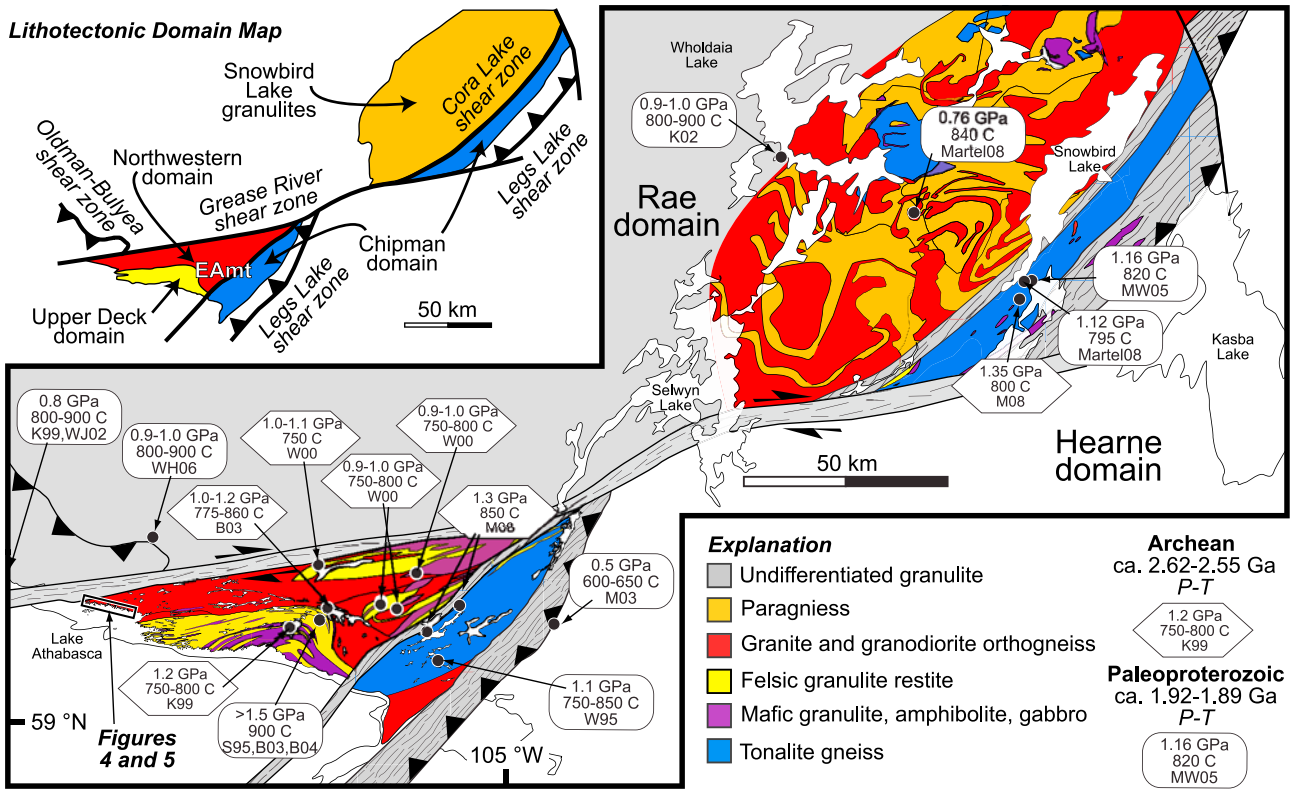

Figure 2. Map of Athabasca granulite terrane with location of transect (Figures 4 and 5) at lower left hand corner (modified after *Mahan et al.* [2008]). Map compiled from *Hanmer* [1994] and *Martel and Pierce* [2006]. Thermobarometric data are keyed to the following references: W95, *Williams et al.* [1995]; S95, *Snoeyenbos et al.* [1995]; K99, *Kopf* [1999]; W00, *Williams et al.* [2000]; K02, *Krikorian* [2002]; WJ02, *Williams and Jercinovic* [2002]; B03, B04, *Baldwin et al.* [2003, 2004]; M03, *Mahan et al.* [2003]; MW05, *Mahan and Williams* [2005]; WH06, *Williams and Hanmer* [2006]; Martel08, *Martel et al.* [2008]; M08, *Mahan et al.* [2008].

2007; *Dumond et al.*, 2008; *Flowers et al.*, 2006a, 2008; *Hanmer et al.*, 1994; *Mahan and Williams*, 2005; *Mahan et al.*, 2006a, 2006b, 2008; *Martel et al.*, 2008].

2.2. East Athabasca Mylonite Triangle

[9] The East Athabasca mylonite triangle (EAMT) (Tantato domain of *Slimmon* [1989]) represents the most thoroughly studied portion of the Athabasca granulite terrane. The EAMT is divided into three lithotectonic domains separated by four high-strain zone boundaries (Figure 2) [*Hanmer*, 1997; *Williams and Hanmer*, 2006]: the Chipman, Upper Deck, and Northwestern domains. The Legs Lake and Grease River shear zones define the eastern and western boundaries of the EAMT, respectively (Figure 2) [*Hanmer et al.*, 1994; *Mahan and Williams*, 2005].

2.2.1. Chipman Domain

[10] The Chipman domain is underlain by the >3.2 Ga Chipman tonalite batholith, the circa 2.59 Ga Fehr granite, the Chipman mafic dike swarm [*Macdonald*, 1980], and discontinuous kilometer-scale sheets of Grt-rich felsic and mafic granulite with minor pyroxenite (Figure 2) [*Hanmer*, 1994]. The dike swarm consists of 1 to 100 m thick amphibole + plagioclase + garnet + clinopyroxene mafic dikes that were locally partially melted, preserving a record of garnet-restite and tonalitic melt production at 1.0–1.2 GPa and 750–850°C [*Williams et al.*, 1995]. Emplacement and partial melting of the dikes occurred in association with steep NE striking fabric development (S_2) at 1.896 Ga [*Flowers et al.*, 2006a]. The western Chipman domain hosts poly metamorphic mafic granulites that record two episodes of HP-HT (high pressure–high temperature) metamorphism at 1.3 GPa, 850–900°C, and 1.0 GPa, 800–900°C [*Mahan et al.*, 2008]. The first episode is linked to production of an early, gently dipping gneissic fabric (S_1) at circa 2.55 Ga, and the second lower pressure event is interpreted to coincide with steep S_2 strain and dike emplacement at circa 1.9 Ga [*Flowers et al.*, 2008; *Mahan et al.*, 2008].

[11] The western boundary of the Chipman domain is juxtaposed adjacent to the Upper Deck and Northwestern domains along the NE striking, steeply NW dipping Cora Lake shear zone [*Johnston*, 1963; *Mahan et al.*, 2008]. The history of the structure is poorly understood, although field relationships are consistent with a component of dextral displacement during D_2 strain at circa 1.9 Ga [*Mahan et al.*, 2008].

2.2.2. Upper Deck Domain

[12] The Upper Deck domain structurally overlies the Northwestern domain along a shallowly SW dipping, top-to-the-SW, ductile shear zone (Figure 2) [*Hanmer et al.*, 1995]. The Upper Deck domain consists of felsic and mafic granulite gneisses with discontinuous lenses of eclogite that record temperatures of 750–1000°C and pressures in excess of 1.5 GPa prior to their juxtaposition with the rest of the EAMT [*Baldwin et al.*2003, 2004, 2007; *Snoeyenbos et al.*, 1995]. High-temperature eclogite facies metamorphism has most recently been interpreted at 1.904 Ga [*Baldwin et al.*, 2004; 2007], although previous workers have inferred a Neoarchean age [*Snoeyenbos et al.*, 1995]. Monazite geochronology by isotope dilution–thermal ionization mass spectrometry (ID-TIMS) and electron probe microanalyzer (EPMA) in the felsic granulite gneisses is consistent with melting and garnet-restite production at circa 2.62–2.55 Ga [*Baldwin et al.*, 2006; *Dumond et al.*, 2007]. In situ analysis of monazite by EPMA in oriented samples of felsic granulite constrains the timing of subhorizontal S_1 fabrics to be synchronous with melting at circa 2.62–2.55 Ga in the Upper Deck domain [*Dumond et al.*, 2007]. Circa 1.9 Ga synkinematic monazite domains document a component of steep, NE striking dextral strike-slip S_2 strain [*Dumond et al.*, 2007], compatible with movement along the Grease River shear zone at circa 1.9 Ga [*Dumond et al.*, 2008].

2.2.3. Northwestern Domain

[13] The Northwestern domain is dominantly composed of felsic to mafic plutonic bodies bounded on their western margin by the Grease River shear zone (Figure 2). The largest body is the circa 2.63–2.6 Ga multiphase Mary batholith [*Hanmer et al.*, 1994; *Hanmer*, 1997]. Granitoids of the Mary batholith were emplaced, metamorphosed, and deformed at ~1.0 GPa, 700–800°C, and locally document the progressive transition from charnockite granitoid to garnet granulite gneiss [*Williams et al.*, 2000]. The northern part of the domain consists of the circa 2.62–2.60 Ga Bohica mafic complex, a suite of gabbroic mafic granulites and anorthosites that are interlayered with the Mary batholith (Figure 2) [*Hanmer et al.*, 1994]. Isolated meter- to kilometer-scale lenses of garnetiferous mafic and felsic granulites also occur throughout the Mary batholith.

[14] Some of the best exposures of the early, subhorizontal S_1 fabric occur in the Northwestern domain of the EAMT (Figure 3). Prior to this study, however, the timing and relationship of S_1 strain to lower crustal HP metamorphism remained poorly understood. This study focuses on subhorizontal fabric development in orthogneisses and felsic granulites of the Northwestern domain. Observations discussed below have been made throughout the EAMT, but we focus on one segment of an across-strike section preserved along easternmost Lake Athabasca (Figures 2–5). Kilometer-scale, D_2 dextral high-strain zones define the western and eastern boundaries of the transect (Figures 4 and 5; see section 3.3). Nearly 100% coastal exposure and

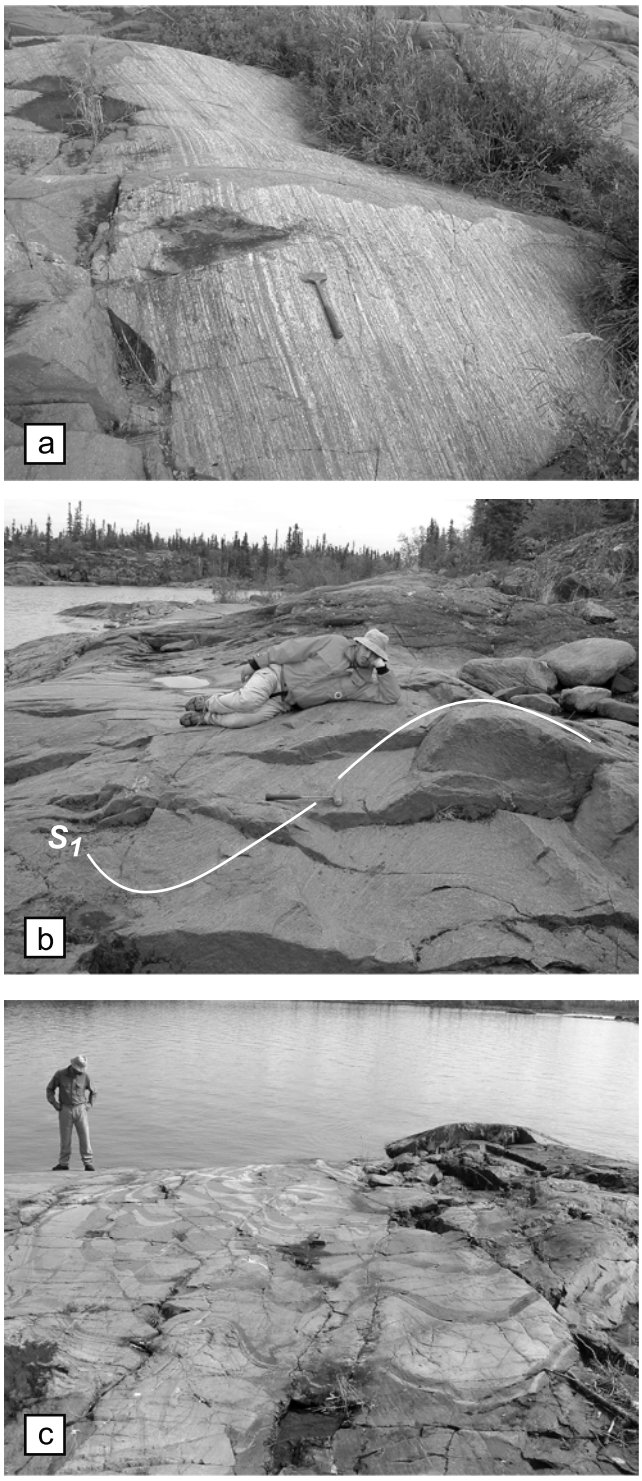

Figure 3. Examples of subhorizontal gneissic fabric in the Mary batholith. (a) Undulating S_1 foliation surface with penetrative striping lineation developed in thin granite sheet. Note highly noncylindrical nature of late folds due to subtle development of dome-and-basin fold interference pattern. See text for discussion. (b) Late, upright open folds of S_1 gneissosity. (c) Heterogeneously layered granodiorite orthogneiss. The enveloping surface of S_1 layering dips away from the viewer of the photograph ~12° toward the NE.

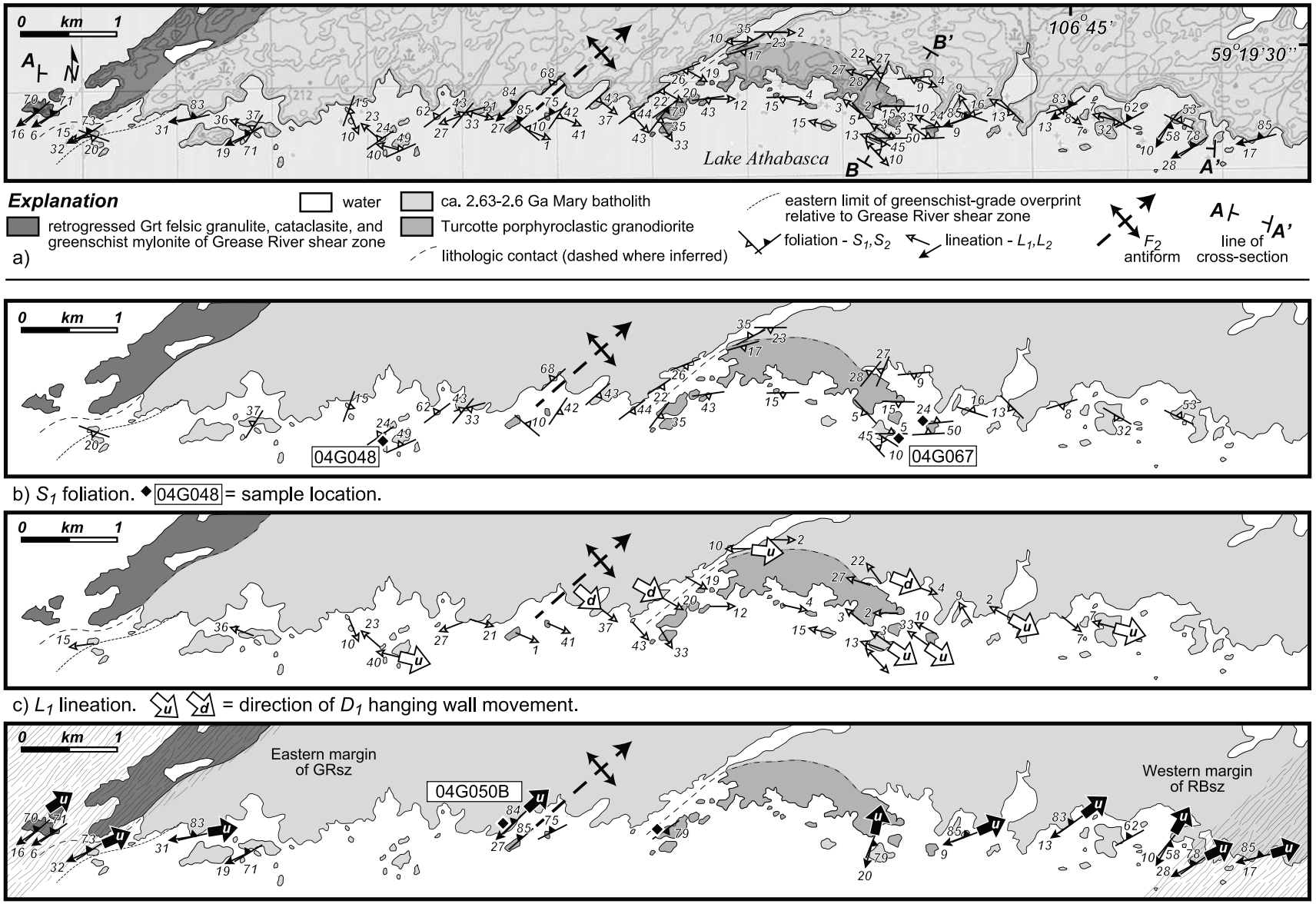

Figure 4. Transect with structural data and sample locations. (a) Geologic map of transect. (b) S_1 foliations and L_1 lineations. (c) Hanging wall movement map for D_1 strain. (d) S_2 foliations and L_2 lineations with D_2 hanging wall movement.

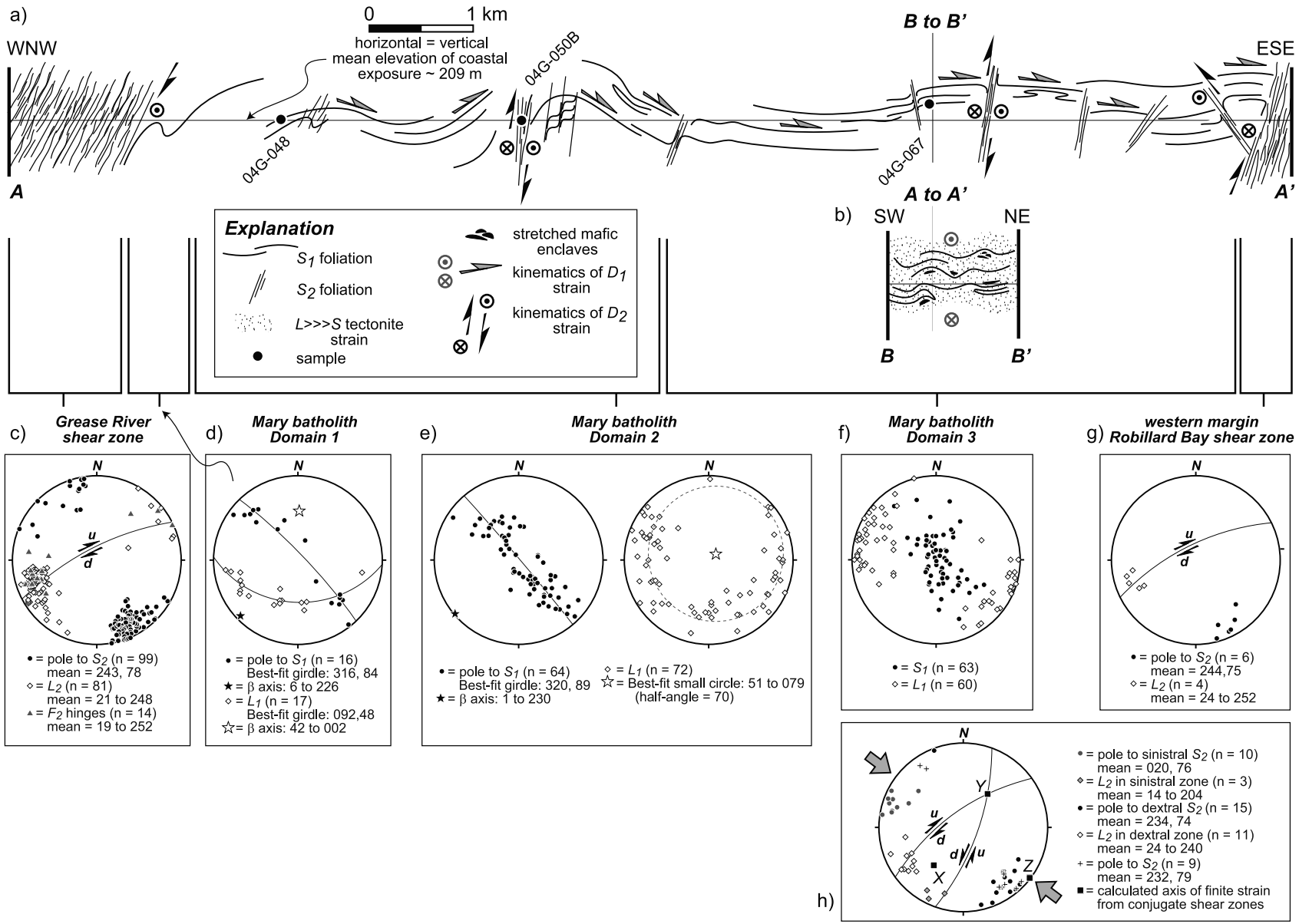

Figure 5. (a) Cross section A-A′ subparallel to L_1 with sample locations. (b) Cross section B-B′ subperpendicular to L_1. (c–g) Stereonets summarizing data for domains along transect discussed in text. (h) Stereonet for D_2 finite strain field.

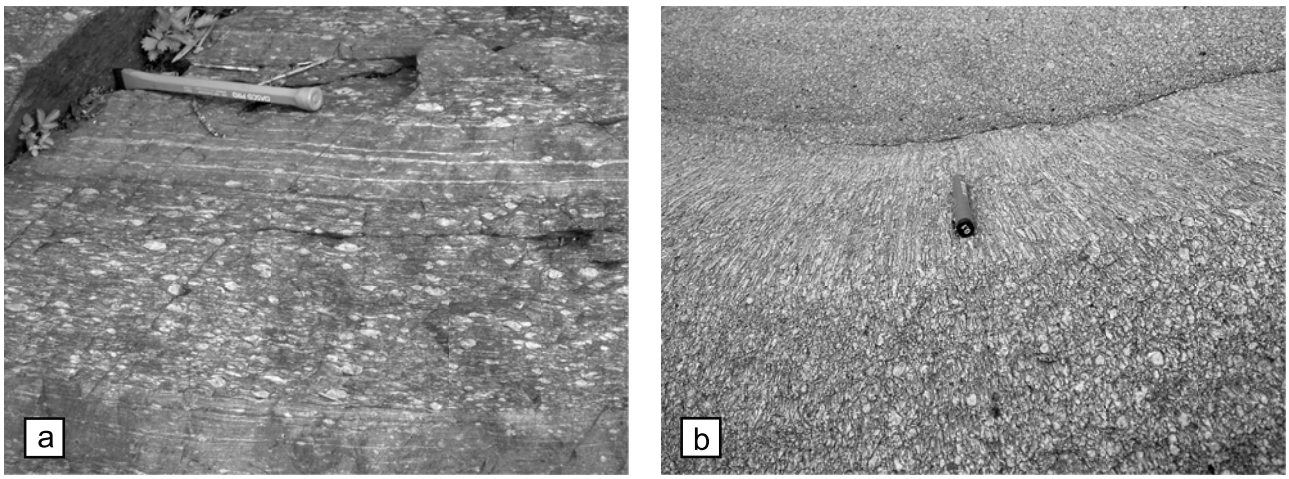

Figure 6. Lithological and macrostructural character of subhorizontal gniessic fabrics in the Mary batholith. (a) Banded mylonitic straight gneisses of the Turcotte granodiorite with porphyroclast-rich and porphyroclast-poor horizons. (b) Penetrative L-tectonite strain from domain 3 along transect in Figures 5a and 5b.

abundant islands afford excellent three-dimensional outcrop control on structures and fabrics (Figures 3 and 4).

3. Structural and Kinematic Constraints on Early Subhorizontal Fabrics in the Mary Batholith

[15] The 12 km long across-strike transect in granitoid orthogneisses and felsic granulites of the Mary batholith is characterized by kilometer- to meter-scale domains of subhorizontal to gently dipping, banded gneissic foliation (S_1) with a penetrative striping lineation (L_1) (Figures 4a and 4b). Sheets of garnet-rich felsic granulite also contain the S_1 gneissic fabric and outcrop throughout the transect, though are not depicted at the scale of Figures 4 and 5. We subdivide the transect into three structural domains based on the orientations of the S_1 and L_1 fabrics (Figures 4 and 5). Orientations of S_1 in domains 1 and 2 define NW striking girdles with subhorizontal β axes consistent with NE trending hinges of F_2 folds that are subparallel to the Grease River shear zone (GRSZ) (e.g., Figures 3b, 3c, 5a, and 5c–5e). Domain 3 is characterized by the best preservation of subhorizontal S_1 foliation and enveloping surfaces, farthest removed from the GRSZ (e.g., Figures 3a, 5a, 5b, and 5f).

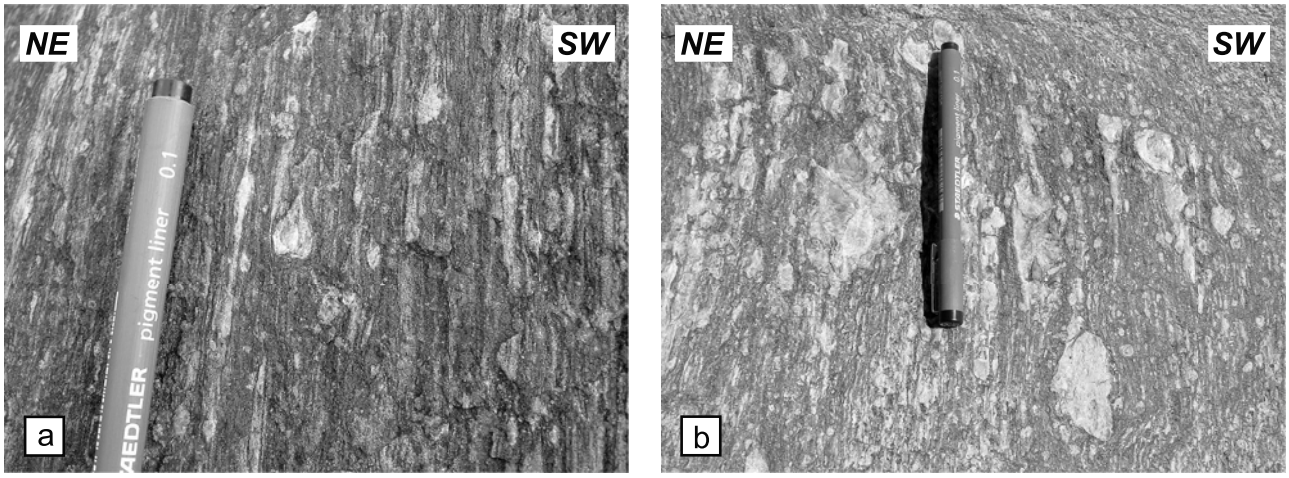

Figure 7. Penetrative L_1 intersection/stretching lineations in the Mary batholith. (a) Elongate white ribbons and mantled porphyroclasts of plagioclase with black stripes of recrystallized amphibole in the Mary granodiorite orthogneiss. The tapered, tear drop shape of the plagioclase clast at center is consistent with top-to-the-ESE kinematics (see text and Figure 8). (b) Large porphyroclasts and ribbons of K-feldspar in the hinge of an F_2 synform.

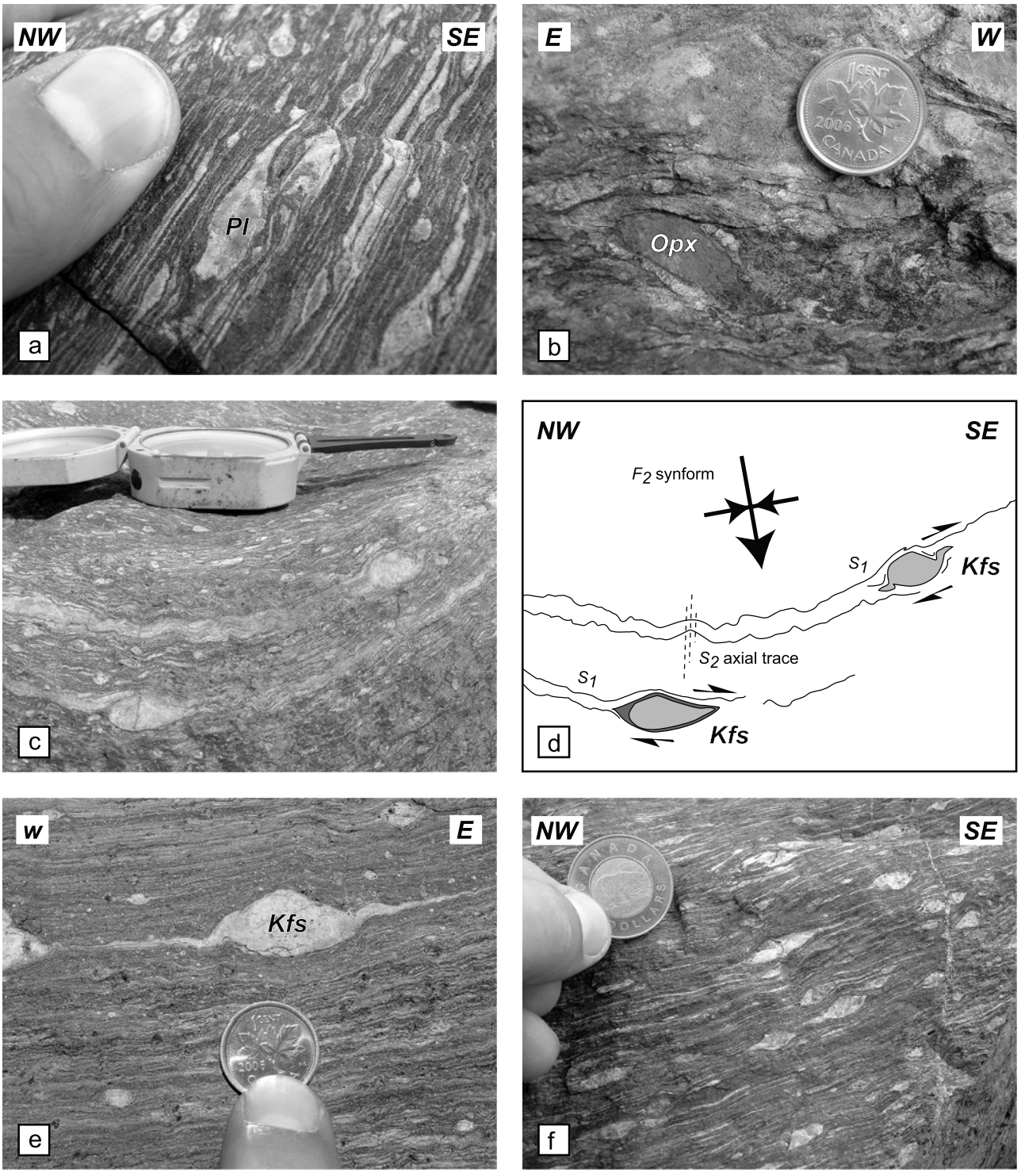

Figure 8. (a–c and e–f) Porphyroclast kinematic indicators observed along the transect, all viewed parallel to L_1 and perpendicular to S_1. Note that Figure 7a is a view of the foliation surface perpendicular to the view in Figure 8a. (d) Sketch of field observations depicting S_1-related top-to-the-SE flow preserved around the hinge of an open F_2 synform in Figure 8c.

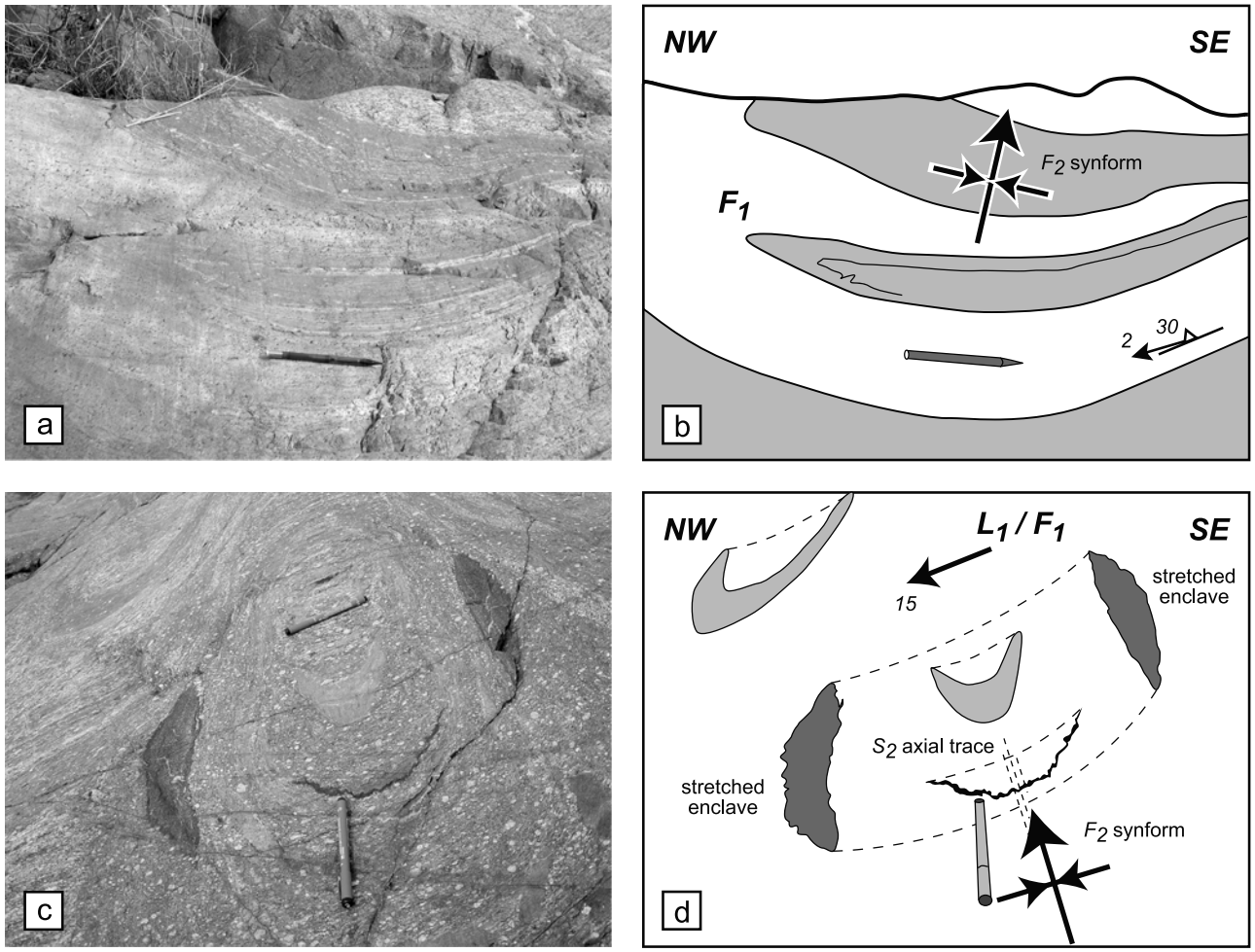

Figure 9. Structures observed parallel to L_1. (a and b) Isoclinal, recumbent F_1 fold with hinge coaxial with L_1 in Mary garnet granodiorite orthogneiss. (c and d) Isoclinal, recumbent F_1 folds with mafic enclaves stretched along L_1. Note overprinting by S_2 and type 2 mushroom-crescent fold interference pattern.

[16] L_1 lineations throughout the transect are variably overprinted by D_2 structures, although D_2 overprinting is demonstrably minor in many parts of the transect (see section 3.3), thus permitting direct examination of the geometry and tectonic significance of D_1 structures (e.g., Figures 3 and 6–11). Domain 3 preserves the least modified orientations of L_1, with dominantly 0–30° plunges and NW-to-SE trends (Figure 5f). Meter-scale corrugations of S_1 and isoclinal folds (F_1) of granite/granodiorite/charnockite sheets (S_0) define hinges that are coaxial with L_1 throughout domain 3 (Figure 5b). Although there is local evidence for a tectonic fabric folded around F_1 hinges, we reserve the use of S_1 for the main penetrative, gently dipping fabric throughout the transect. L_1 lineations in domain 2 define a small-circle distribution consistent with folding of a preexisting line via buckling (Figures 5e and 5f) [*Ramsay*, 1967]. Lineations in domain 1 in the footwall of the Grease River shear zone, however, plot along a great circle that is oblique to F_2 folds, consistent with folding that involved a component of heterogeneous subsimple shear [e.g., *Ramsay*, 1967].

3.1. S_1 Fabric: L ≫ S to L-Tectonite

[17] The S_1 fabric is mylonitic at all scales of observation. Gneissic foliation is defined by ribbons of K-feldspar + plagioclase and flattened, elongate porphyroclasts (<1 to 7 cm in length) of K-feldspar and plagioclase with well-developed core-and-mantle structures (Figures 6a, 7, and 8). The foliation is also defined by sigmoidal porphyroclasts of orthopyroxene (up to 3 cm in length) (Figure 8b), aggregates of garnet, recrystallized laths of amphibole, ribbons of quartz, and late biotite. Centimeter- to decimeter-scale compositional layering (i.e., defined by orthogneisses of different bulk compositions) is commonly subparallel to S_1 (Figures 3c and 6a), except where intrusive relationships are overprinted by the S_1 foliation (Figure 10a). Sheets of migmatitic garnet-rich felsic granulite (tens of m in thickness) also contain the penetrative gneissic fabric as defined by ribbons of quartz and

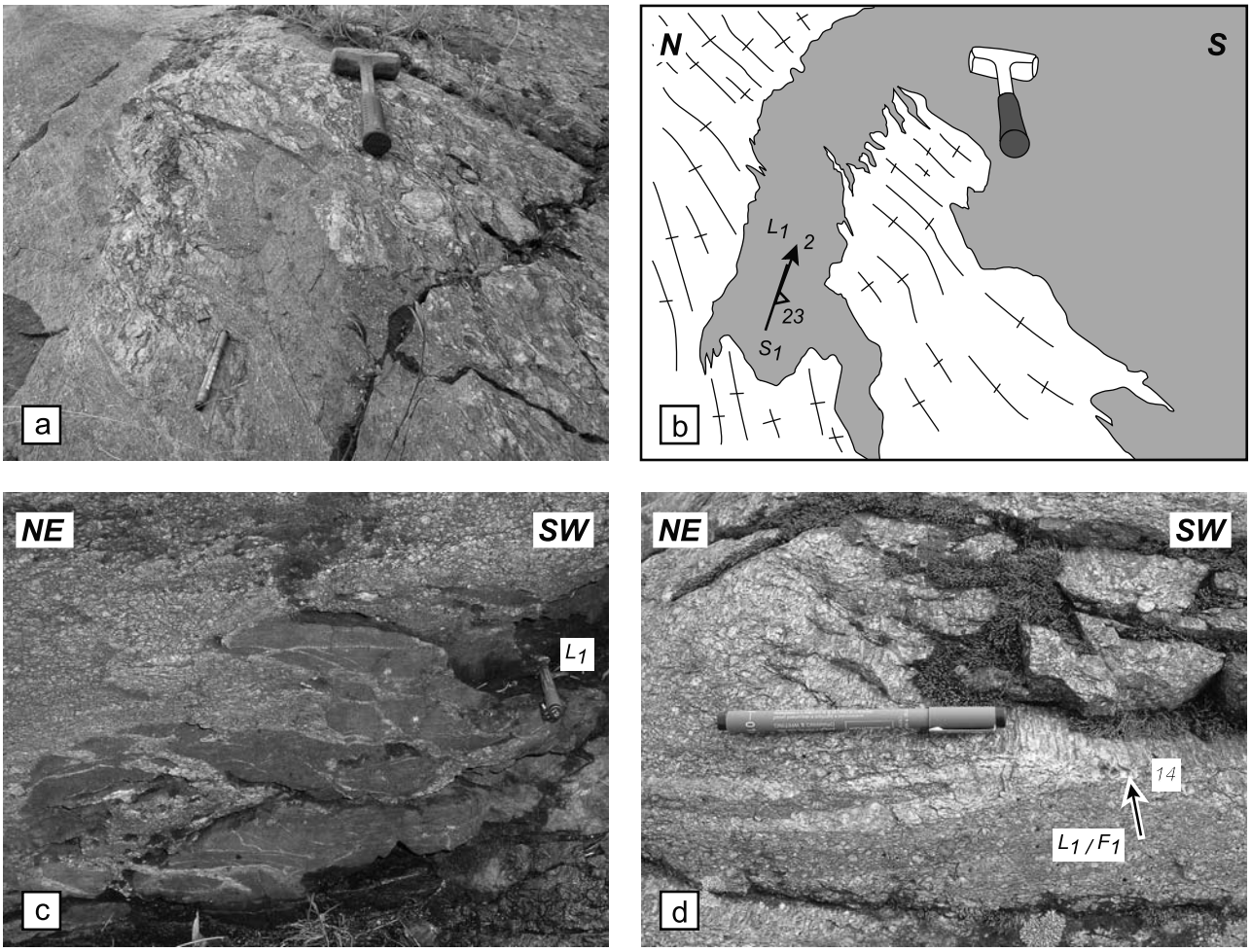

Figure 10. Structures observed perpendicular to L_1 and along the transect. (a and b) Pegmatitic apophysis of Opx-bearing granitoid (charnockite) with delicate, interfingering intrusive contacts with the host granodiorite, subsequently overprinted by penetrative S_1 foliation. c) Downplunge view of net-veined mafic enclaves flattened and sheared subparallel to S_1 and L_1. d) Downplunge view of recumbent, isoclinal F_1 fold with hinge coaxial to L_1.

recrystallized porphyroclasts of plagioclase + K-feldspar (not shown at the scale of the map in Figure 4). The recrystallized character of the fabric and the effects of grain size reduction are well preserved in all lithologies, with only localized development of post-S_1 coarsening and annealing in amphibole-rich orthogneisses and felsic granulites.

[18] D_1 strain is heterogeneously distributed at the transect scale (Figure 5) and locally at the outcrop scale (Figures 6, 9, and 10). Penetrative L > S tectonites dominate the western half of the transect (i.e., domains 1 and 2; see Figures 5a, 5d, and 5e). L $\gg$ S to L-tectonites are more characteristic of the eastern half of the transect (i.e., domain 3: Figures 5a, 5b, and 5f). Fabrics at the outcrop scale also vary in character with porphyroclast-poor, straight-banded gneisses interlayered with porphyroclast-rich horizons (Figure 6a). Relict compositional layering is subtle to virtually absent in L-tectonite zones (Figure 6b). Observations of the S_1-L_1 fabric are consistent with penetrative subhorizontal general shear strain manifested in protomylonitic- to ultramylonitic-banded orthogneisses and migmatitic felsic granulites.

3.2. L_1: A Two-Component Mineral Lineation

[19] Subhorizontal to gently plunging L_1 lineations are defined by two components (Figure 7). The first consists of discontinuous ribbons of recrystallized K-feldspar + plagioclase + quartz + amphibole ± orthopyroxene, aggregates of garnet, and millimeter- to centimeter-scale core-and-mantle structures defined by tapered clasts of K-feldspar and plagioclase. The second component is defined by subcontinuous, tens of centimeters long monomineralic and polymineralic rods or stripes of K-feldspar + plagioclase + quartz ± amphibole. In outcrop, some of the subcontinuous stripes can be traced to isoclinally folded (F_1) layers of granodiorite/granite/charnockite (S_0) that are observed perpendicular to L_1. These observations are consistent with a mineral lineation that is both a stretching lineation and an

intersection lineation of an earlier fabric (S_0). These characteristics persist on the limbs (Figure 7a) and in the hinge zones of open to tight F_2 folds (Figure 7b). Sections 3.2.1 and 3.2.2 describe aspects of the composite lineation in detail, focusing on kinematics and structures observed parallel and perpendicular to L_1.

3.2.1. Kinematics Parallel to L_1 and Perpendicular to S_1

[20] Porphyroclast kinematic indicators are abundant in planes of view parallel to L_1 and perpendicular to S_1 (Figure 8) [e.g., *Passchier and Trouw*, 2005]. Plagioclase and K-feldspar represent the most common porphyroclast phases, typically defining flattened σ- and δ-type core-and-mantle structures with millimeter-scale poly to monocrystalline mantles readily observable in outcrop (Figures 8a and 8c–8f). Orthopyroxene occurs less commonly and defines tapered, elongate σ clasts (Figure 8b).

[21] Figure 8 illustrates σ- and δ-type clasts identified in orthogneisses from west to east along section A-A′ in Figure 5. Plagioclase porphyroclasts identified in the western limb of the map-scale F_2 antiform in Figure 5a (domain 2) record top-up-to-the-ESE displacement (Figure 8a). Orthopyroxene σ clasts observed in the eastern limb, in addition to ubiquitous feldspar porphyroclasts, document top-down-to-the-ESE displacement (Figures 5a and 8b). Domain 3 provides access to kinematics that are least modified by D_2 strain in outcrops further east (Figure 5a; compare Figures 5d–5f). Top-to-the-ESE kinematics defined by feldspar porphyroclasts persist in the hinges of broad, low-amplitude F_2 folds and warps. On subhorizontal S_1 foliation (Figure 8e) and variably NE and SW dipping S_1 foliation in domain 3 (e.g., Figure 8f), kinematics remain top-to-the-ESE along L_1.

[22] A summary of kinematics resolved along L_1 relative to S_1 at several outcrops is depicted in a hanging wall movement map (Figure 4c). The map and sections A-A′ and B-B′ (Figures 5a and 5b) illustrate the consistent top-to-the-ESE kinematics for D_1 strain throughout the study area, precluding any appreciable overprinting due to flexural flow during F_2 folding. Coupled with observations in the least modified domain 3 (Figures 5a and 5f), the results are most consistent with penetrative subhorizontal, top-to-the-ESE regional-scale ductile flow during D_1 strain at the transect scale (over $\sim$20 km^2 area).

3.2.2. Structures Observed Parallel and Perpendicular to L_1

[23] Three-dimensional outcrop exposures and abundant map view exposures inclined to S_1 permit observations of macroscale structures parallel to L_1 (Figure 9). The S_1 fabrics locally define isoclinally folded sheets (F_1) of granite/granodiorite/charnockite (Figures 9a, 9b, and 10d). Hinges of F_1 folds are coaxial with L_1 (Figures 9 and 10d). Decimeter-scale, mafic enclaves with high-aspect ratios are also elongated with long axes parallel to L_1 (Figures 9c and 9d).

[24] Exposures perpendicular to L_1 locally reveal structures related to the magmatic history of the porphyroclastic orthogneisses (Figures 10a and 10b), whereas other exposures (particularly in domain 3) reveal a record of L-tectonite strain and corrugation development (see below) (e.g., Figures 5b and 6b). Pegmatitic apophyses of Opx-bearing granitoid (charnockite) contain delicate, interfingering intrusive contacts with the host granodiorite, subsequently overprinted by penetrative S_1 foliation (Figures 10a and 10b). Net-veined mafic enclaves are flattened and sheared subparallel to S_1 and L_1 (Figure 10c).

[25] Well-developed map- and outcrop-scale upright corrugations of S_1 and F_1 folds occur along a transect perpendicular to L_1 in domain 3 (section B-B′ in Figures 4a and 5b). The open corrugations are coaxial with L_1 and have subvertical, NW striking axial planes (Figure 5b). Penetrative cleavage is notably absent in the low-amplitude, tens of meter-scale corrugations. The geometry of the corrugations are most consistent with a component of *y* axis shortening and constriction during the waning stages of D_1 strain and $L \ggg S$ tectonite development [i.e., *Fletcher and Bartley*, 1994; *Mancktelow and Pavlis*, 1994].

3.3. Overprinting of S_1/L_1 Fabric

[26] Overprinting of the S_1-L_1 fabric at the transect scale (Figure 5a) is represented by NE striking, steeply NW dipping D_2 dextral shear zones that bound the transect and upright open to tight F_2 folds with subhorizontal enveloping surfaces in domains 1 and 2 (Figures 4a and 5). The 5 to 7 km wide Grease River shear zone [*Gilboy*, 1980] marks the western margin of the transect and contains a shallowly SW plunging stretching lineation that is coaxial with tight to isoclinal F_2 folds and sheath folds (Figure 5c). Kinematic indicators throughout the Grease River shear zone are uniformly dextral as defined by C′ shear bands and abundant δ and σ clasts of K-feldspar and plagioclase [*Dumond et al.*, 2008; *Hanmer*, 1997; *Slimmon*, 1989]. The locally ultramylonitic Robillard Bay shear zone defines the eastern margin of the transect (Figure 5a), strikes subparallel to the Grease River shear zone, and also contains a shallowly SW plunging stretching lineation with dextral, highly oblique-slip kinematics defined by feldspar δ clasts and rotated mafic enclaves (Figure 11f). Subhorizontal to shallowly plunging F_2 hinges throughout domains 1–3 trend subparallel to the bounding shear zones (e.g., compare β axes in Figures 5d and 5e with Figure 5c).

[27] Outcrop-scale overprinting is characterized by (1) upright, open F_2 folds with rare S_2 axial planar cleavage, (2) kinking and buckling of the S_1 fabric subperpendicular to L_1, (3) local development of type 1 and 2 fold interference patterns, and (4) penetrative, centimeter to tens of meters thick NE striking, steeply dipping high-strain zones. Generally low-amplitude, upright open F_2 folds and warps of the S_1 gneissic fabric are observed throughout the transect (e.g., Figure 3b). Minor folds in the Mary batholith become tight nearest to the GRSZ, although the L_1 lineation is still preserved on both limbs (Figure 11a; domain 1 in Figures 5a and 5d). Penetrative cleavage is rare, and best developed as a spaced crenulation cleavage in the hinges of F_2 folds in domain 2 (Figures 5a and 11b). Variably developed kinking or buckling of the S_1 fabric is present in all domains along the transect (e.g., Figures 8c, 8d, and 11c). Chevron-shaped kinks are best observed in planes parallel to L_1 and perpendicular to S_1 (Figure 11c), with the axial plane of the kinks occurring perpendicular to L_1 and subparallel to the S_2 cleavage. Domains 2 and 3 locally preserve type 2

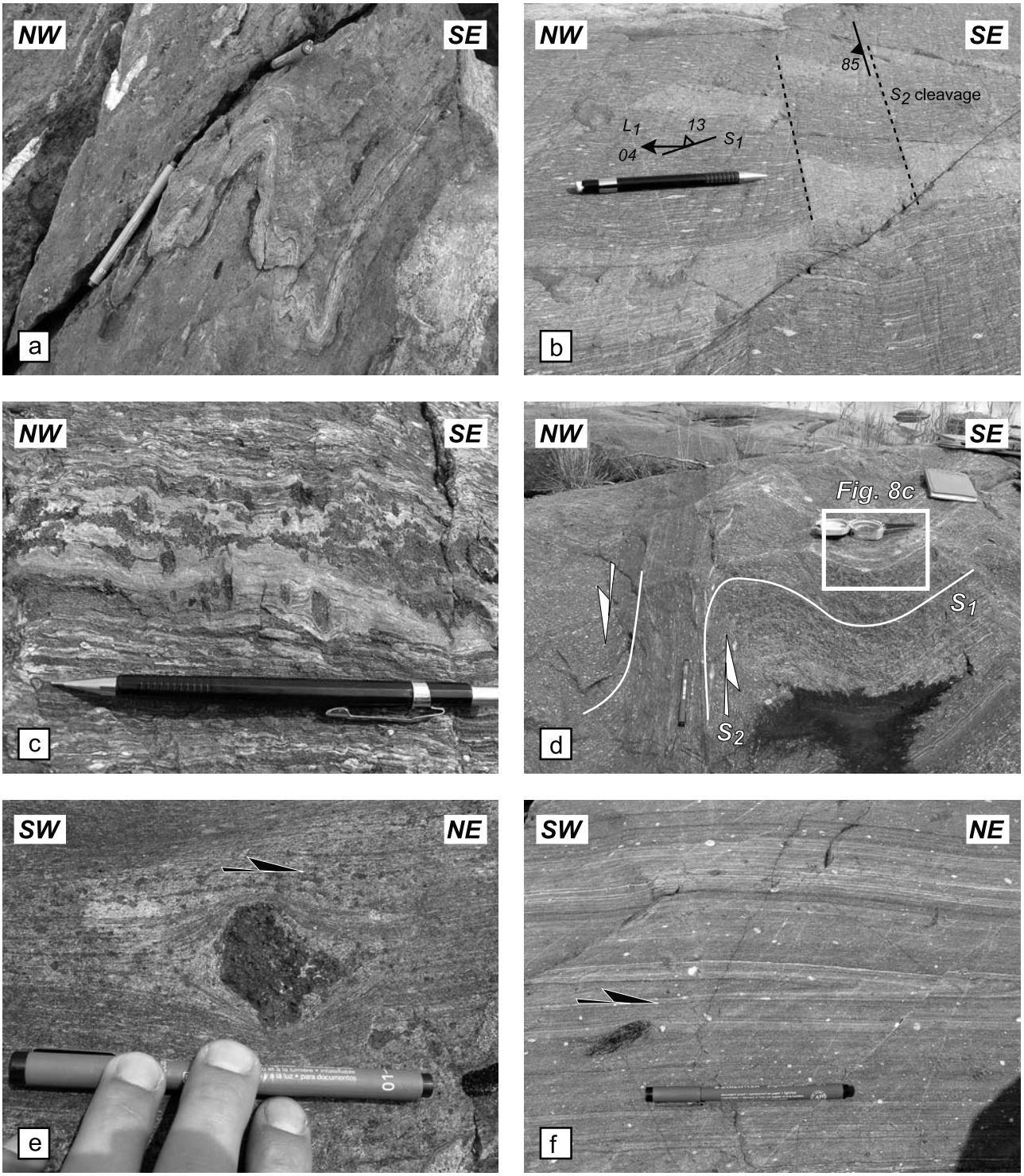

Figure 11. Overprinting by D_2 strain along the transect. (a) Tight, upright F_2 folds in Mary granodiorite gneiss near Grease River shear zone with L_1 preserved on limbs. (b) Spaced S_2 cleavage cutting subhorizontal S_1 and L_1. (c) Buckling of S_1 around retrogressed garnet porphryoblasts in migmatitic felsic granulite. (d) Less common discrete D_2 sinistral shear zone. Note transposition of fabric and location of Figures 8c and 8d. (e) Mantled garnet porphryoblast in dextral mylonite on western margin of map-scale antiform in Figures 4 and 5 where sample 04G-050B was acquired. (f) Ultramylonite and mafic enclave dextral δ clast in the western margin of the Robillard Bay shear zone.

(mushroom-crescent) fold interference patterns resulting from superposition of upright F_2 folds with subvertical NE striking axial planes onto isoclinal, recumbent F_1 folds (Figures 9a and 9c) [*Ramsay and Huber*, 1987]. Type 1 (dome-and-basin) fold interference patterns due to superposition of F_2 folds onto upright, NW striking D_1 corrugations occur less commonly (Figure 3a) [*Ramsay and Huber*, 1987]. Numerous centimeter- to tens of meter-scale dextral, steep high-strain zones and a minor amount of sinistral high-strain zones (Figure 11d) occur sporadically throughout domains 2 and 3 (Figure 5a). In high-strain zones, S_1 is reoriented into steeply dipping, NE striking domains characterized by complete transposition of L_1 into a shallowly SW plunging L_2 lineation defined by recrystallized K-feldspar, plagioclase, amphibole, and quartz (Figure 11d). This phenomenon is best illustrated in the NW limb of the map-scale antiform in domain 2 (Figures 4a and 5a) where S_2 strain localized into a tens of meters wide dextral shear zone (Figure 11e).

[28] The kinematics of D_2 strain throughout the Mary batholith are dominantly dextral, top-to-the-NE as defined by mantled porphyroclasts of K-feldspar, plagioclase, and garnet (see D_2 hanging wall movement in Figures 4d, 11e, and 11f). Minor sinistral shear zones may be conjugate, with the dextral sense being more dominant (Figure 5h). Calculation of the acute bisectrix of the mean orientations of these zones [after *Ramsay and Huber*, 1983] yields axes of finite strain consistent with NW–SE subhorizontal contraction and a SW plunging extension direction (Figure 5h), kinematically compatible with observations along the Grease River shear zone [*Dumond et al.*, 2008].

4. Microstructural Observations of Penetrative Subhorizontal S_1 Tectonite

[29] Microstructural observations provide insights into the deformation mechanisms and metamorphic grade associated with development of the penetrative subhorizontal S_1 tectonite. *Williams et al.* [2000] mapped steeply dipping D_2 strain gradients in the core of the Mary batholith and focused on the development of nonmigmatitic gneissic layering in Opx-bearing orthogneisses. The work was done prior to any recognition of the significance of the subhorizontal S_1 fabrics illustrated in this study. New microstructural data are presented below from amphibole ± garnet-bearing orthogneisses that contain the S_1 gneissic fabric (Figure 12).

4.1. Garnet + Amphibole Granodiorite Orthogneisses

[30] Much of the transect is underlain by a compositionally heterogeneous suite of garnet + amphibole-bearing granodioritic orthogneisses (e.g., sample 04G-048 located in domain 2 of the Mary batholith in Figures 4b and 5a). The rocks display <0.3–2 mm thick gneissic layering defined by alternating horizons of dynamically recrystallized plagioclase + K-feldspar + quartz and amphibole + ilmenite. The banded gneisses are porphyroclastic, with flattened and mantled σ- and δ-type clasts of plagioclase and K-feldspar (Figure 12a) [e.g., *Passchier and Trouw*, 2005]. Gneissic layering also consists of monocrystalline ribbons of K-feldspar, plagioclase, and quartz with aspect ratios up to 30:1. Rare relict cores in K-feldspar ribbons are composed entirely of subgrains, and the margins of the cores define highly lobate boundaries adjacent to a mantle of recrystallized grains, indicative of subgrain rotation recrystallization (Figure 12b). Cuspate-lobate grain boundaries between adjacent K-feldspar grains and between K-feldspar and plagioclase grains in the mantle indicate grain boundary migration recrystallization. Lattice preferred orientation is well developed in the vicinity of the cores, but diminishes with distance away from the cores as K-feldspar ribbons become completely recrystallized to grain sizes approaching 20 μm in diameter. Plagioclase cores are better preserved with albite twinning still apparent, overprinted by sweeping undulatory extinction. Calcic cores are mantled by recrystallized new grains of albitic plagioclase, garnet, amphibole, and irregular pools of quartz (Figure 13a). Recrystallized grains in plagioclase mantles are nearly the same size as subgrains in the clasts (as small as 80 μm in diameter) and have a similar lattice preferred orientation, consistent with subgrain rotation recrystallization. Lobate grain boundaries between plagioclase grains and subgrains, in addition to pinning microstructures between amphibole and plagioclase are consistent with grain boundary migration recrystallization (Figure 12c) [*Jessell*, 1987]. Quartz occurs in three settings: (1) as virtually strain-free grains that share lobate grain boundaries with K-feldspar and new plagioclase grains in the strain shadows of relict plagioclase porphyroclasts, (2) as elongate ribbons in the matrix that pinch out on their ends and consist of variably recrystallized single grains, and (3) as long monominerallic veins (200–300 μm wide) with irregular- to straight-sided walls that truncate feldspar grains and extend across the entire thin section, parallel to S_1 [see also *Williams et al.*, 2000].

4.2. Turcotte Amphibole-Bearing Granodiorite Orthogneiss

[31] Sheets of amphibole-bearing orthogneiss occur near the center of the transect, originally mapped as the Turcotte granodiorite by *Hanmer* [1994] (Figure 4a). Contacts between porphyroclast-rich banded gneisses and porphyroclast-poor ultramylonite horizons range from sharp to gradational (Figure 6a). Gneissic banding (<0.1–3 mm thick) is defined by ribbons of K-feldspar + plagioclase + quartz in association with amphibole + titanite + biotite + calcite. Amphibole occurs as isolated recrystallized porphyroclasts in the matrix, and as new grains in the recrystallized mantles of antiperthitic plagioclase. K-feldspar and plagioclase define flattened, mantled δ- and σ-type porphyroclasts (Figure 12e). K-feldspar cores locally exhibit lobate to amoeboid grain boundaries, display undulatory extinction, and contain inclusions of calcite and amphibole. Other K-feldspar cores are completely replaced by subgrains and dissected by zones of new grains with the same lattice preferred orientation, consistent with subgrain rotation recrystallization. Where K-feldspar is completely recrystallized, i.e., where clasts are transformed into ribbons, grain sizes approach 3–4 μm in diameter. Plagioclase clasts

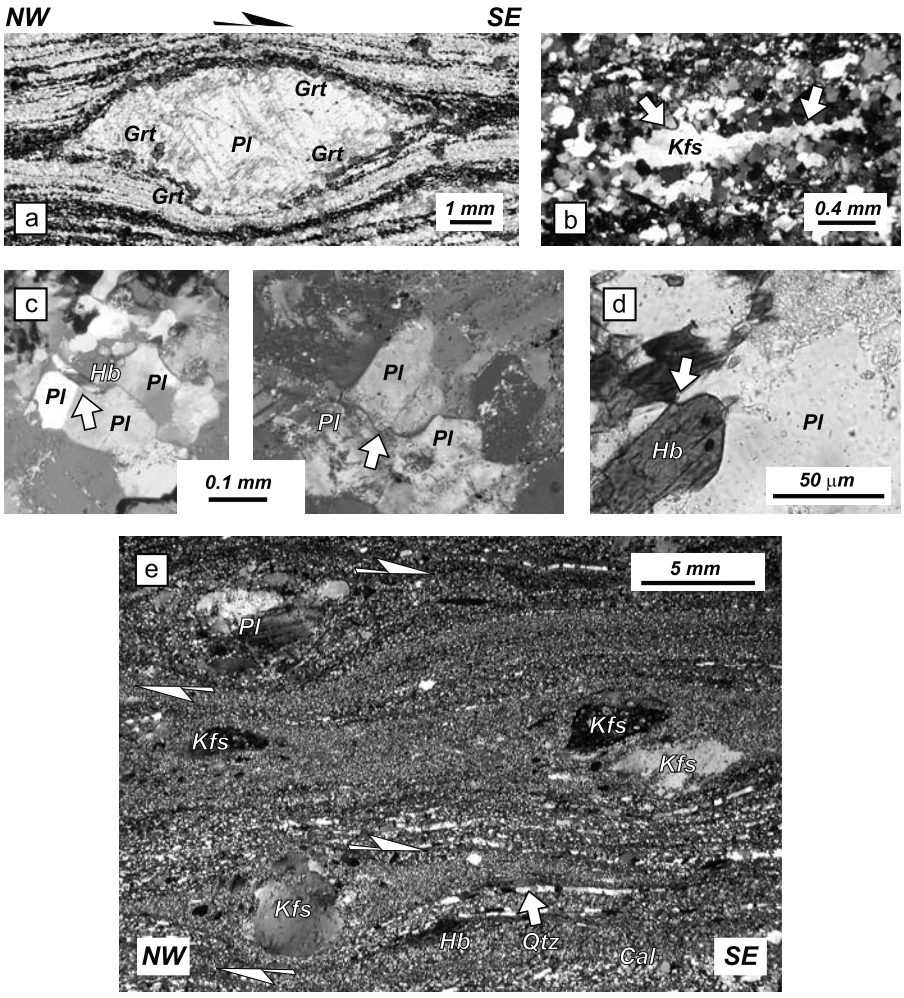

Figure 12. Microstructural observations of subhorizontal S_1 tectonites. (a) Flattened plagioclase porphyroclast with garnet in the recrystallized mantle. (b) Relict, highly lobate core (see arrows) of K-feldspar ribbon filled with subgrains. (c) (left) Pinning microstructures between plagioclase and amphibole (see arrow) and (right) lobate grain boundaries in recrystallized plagioclase (see arrow). Quartz wedge inserted under cross-polarized light. (d) Lobate grain boundary between antiperthitic plagioclase and amphibole indicative of high-temperature grain boundary migration (see arrow). (e) Flattened porphyroclasts, σ- and δ-type clasts of plagioclase, and K-feldspar in Turcotte granodiorite. Note preservation of dramatic grain size reduction with little annealing, in addition to elongate quartz veins (see arrow) and ribbons.

display similar microstructures as K-feldspar, although plagioclase is generally more coarsely recrystallized (down to 10 μm in diameter) and compositionally heterogeneous with calcic cores mantled by sodic rims, as observed in electron probe X-ray maps. Plagioclase rims exhibit lobate intergrowths and pinning microstructures with amphibole, indicative of grain boundary migration recrystallization (Figure 12d) [*Passchier and Trouw*, 2005].

4.3. Microstructural Summary

[32] The microstructural observations discussed above emphasize the roles of subgrain rotation and grain boundary migration recrystallization affecting porphyroclasts of both K-feldspar and plagioclase in the banded orthogneisses. Combined with textural evidence for pervasive ribbon development in K-feldspar + plagioclase + quartz, and evidence for growth of new phases like sodic plagioclase, garnet, and amphibole, the results support the operation of crystal-plastic deformation mechanisms, i.e., dislocation and diffusion creep at high temperature (greater than 650–700°C) [*Passchier and Trouw*, 2005; *Rutter and Brodie*, 1992; *Tullis*, 2002]. The preservation of such fine grain sizes and high-strain microstructures without appreciable annealing, e.g., grains as small as 3–20 μm for K-feldspar and 10–80 μm for plagioclase, requires low activity of H_2O or relatively high activity of CO_2 [*Mancktelow and*

Pennacchioni, 2004], as implied by interstitial calcite in the Turcotte granodiorite.

5. Pressure-Temperature Conditions of S_1

[33] Previous thermobarometric estimates derived from Opx + Cpx + Grt ± Hb granodioritic orthogneisses yielded conditions of 0.9–1.2 GPa and 750–860°C throughout the Mary batholith (shown in Figure 2) [*Baldwin et al.*, 2003; *Williams et al.*, 2000]. The relationship between lower crustal metamorphism and S_1 fabric development, however, remained unconstrained in the Northwestern domain prior to this study. New thermobarometric data from one oriented sample is presented below that permits a direct link between S_1 strain and synkinematic mineral growth (Figure 13). High-resolution X-ray mapping of all phases was carried out prior to analysis with the Cameca SX50 electron probe microanalyzer (EPMA) at the University of Massachusetts. Maps were generated at 15 kV and 150–200 nA with 4–10 μm pixel step sizes and 50–70 ms dwell times. Quantitative analyses, guided by the X-ray maps, were collected at 15 kV and 20 nA with a focused beam for garnet and a defocused beam (5 μm) for plagioclase and amphibole. Count times were 20 counts s^{-1} on peak and 10 counts s^{-1} on background. Calibrations were made using common natural and synthetic standards.

[34] Garnet, amphibole, and plagioclase (all in association with quartz) were analyzed in sample 04G-048, located in the Mary batholith domain 2, to constrain the *P-T* conditions of S_1 (Figure 13 and Table 1). The metamorphic assemblage occurs in the recrystallized mantles of plagioclase δ clasts with the same top-to-the-SE kinematics observed along the transect. Garnet (up to 0.5 mm in diameter) is grossular-rich almandine (Alm_{71}, Grs_{21}, Pyr_{5-6}). High-resolution X-ray maps show little to no zoning. Quantitative line scans reveal slight rimward increases in X_{Fe} and decreases in X_{Mg}, attributed to retrograde diffusional reequilibration (Figure 13b). Plagioclase compositions range from An_{38} in the cores to An_{22} at the rims. Recrystallized matrix plagioclase grains in the vicinity of the porphyroclasts are also An_{22}. Amphibole is ferropargasite according to the classification of *Leake et al.* [2003] and is similar in composition in both the matrix and the porphyroclast mantles. Thermobarometric estimates were made using the core composition of the largest garnet in the plagioclase mantle because it is likely to be the least modified by retrograde cooling. Results were obtained using the avPT method in

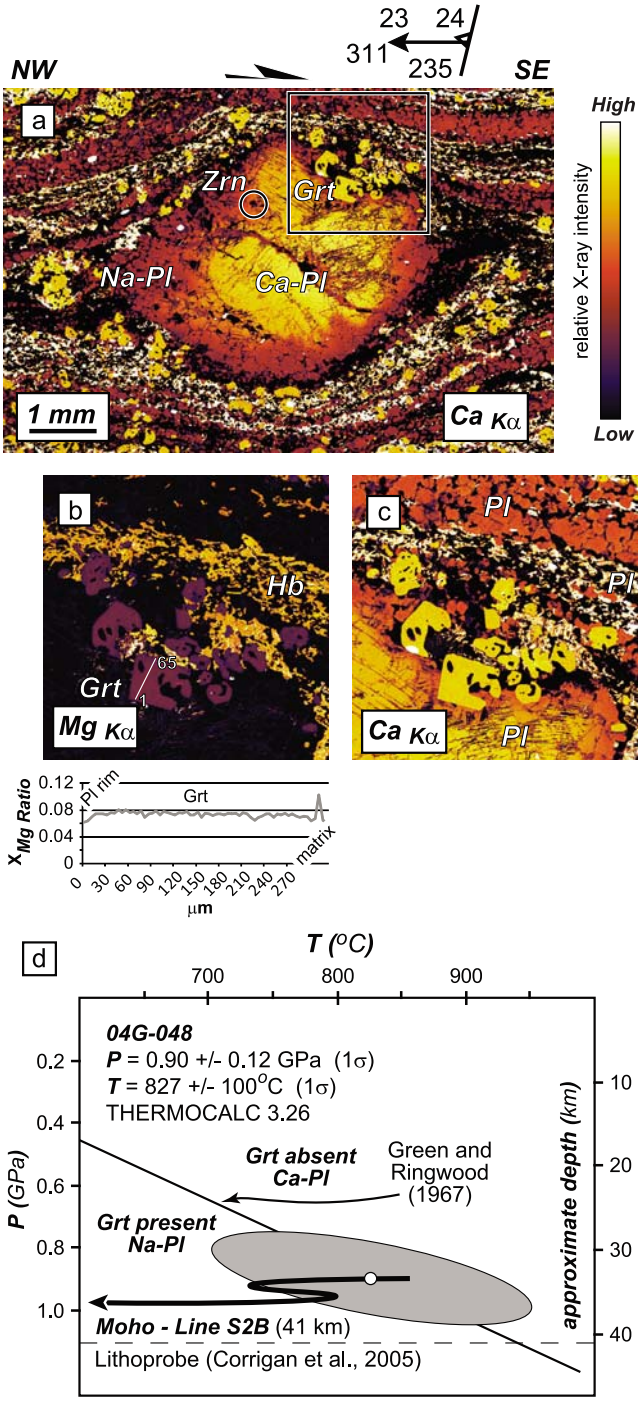

Figure 13. (a) High-resolution EPMA X-ray map of calcic plagioclase porphyroclast illustrating synkinematic character of garnet growth in recrystallized sodic mantle in sample 04G-048. Note top-to-SE kinematics defined by δ clast asymmetry and location of zircon. (b) X-ray map and quantitative line scan depicting homogenous Mg zoning in garnet and amphibole (Hb). Note location of garnet traverse. (c) X-ray map showing growth of garnet in Ca-poor (Na-rich) recrystallized mantle of plagioclase porphyroclast [see also *Williams et al.*, 2000]. (d) Average P-T estimate with 1σ uncertainty ellipse determined from THERMOCALC v.2.6. Near isobaric P-T path of *Williams et al.* [2000] overlain for reference. Grt-present reaction line for quartz tholeite bulk composition from *Green and Ringwood* [1967]. Note depth to Moho beneath Athabasca basin from nearby Lithoprobe seismic reflection line S2B for reference [*Corrigan et al.*, 2005] (line located in Figure 1a as S2B).

Table 1. Mineral Compositions for 04G-048[a]

Oxide (wt %)	Grt	Pl	Hb
FeO	32.83	0.18	25.98
MgO	1.47	NA	3.85
MnO	0.83	NA	0.16
CaO	7.61	4.85	11.46
Na_2O	NA	9.18	1.10
K_2O	NA	0.18	1.27
TiO_2	0.04	NA	1.25
Al_2O_3	21.33	23.72	11.52
SiO_2	37.06	62.34	41.02
Total	101.17	100.44	97.62
	Number of Oxygens		
Cations	12	8	23
Fe	2.190	0.007	3.422
Mg	0.175	NA	0.904
Mn	0.056	NA	0.021
Ca	0.651	0.230	1.934
Na	NA	0.787	0.168
K	NA	0.010	0.128
Ti	0.003	NA	0.296
Al	2.006	1.236	3.207
Si	2.957	2.756	12.920
An		0.224	
Ab		0.767	
Kfs		0.010	
Grs	0.212		
Alm	0.713		
Prp	0.057		

[a]NA, not analyzed. Sample location is UTM E 393143 N 6576473 zone 13V NAD 27.

Thermocalc 3.26 [*Powell and Holland*, 1994] with the November 2003 version of the internally consistent thermodynamic database of *Holland and Powell* [1998]. Activity-composition relationships were modeled at 1.0 GPa and 750°C using the year 2000 version of AX (T. Holland, http://rock.esc.cam.ac.uk/astaff/holland/index.html) and the amphibole model of *Dale et al.* [2000]. Estimates for *P* and *T* were calculated for fluid-undersaturated conditions and yielded the smallest σ_{fit} at an activity of $H_2O = 0.5$. Average *P-T* results indicate conditions of 0.90 ± 0.12 GPa (1σ) at 827 ± 100°C (1σ) (Figure 13d).

[35] The new *P-T* estimates are consistent with the data of *Williams et al.* [2000] and *Baldwin et al.* [2003], revealing a laterally extensive batholith that equilibrated at lower crustal conditions (~30–40 km paleodepths). Retrograde zoning in garnet and textural evidence for garnet growth at the expense of plagioclase is consistent with near-isobaric cooling at depth as inferred for the Mary batholith by *Williams et al.* [2000] (see path in Figure 13d). *Williams et al.* [2000] first observed the preferential nucleation of Ca-rich garnet in the Na-rich mantles of recrystallized plagioclase porphyroclasts during deformation in the Mary batholith. This study demonstrates that growth of garnet and amphibole during synkinematic recrystallization of plagioclase was synchronous with D_1 subhorizontal fabric development at lower crustal depths (Figure 13a and 13d).

6. Timing Constraints on S_1 and S_2

[36] Crystallization ages for various phases of the Mary batholith range from circa 2.63–2.60 Ga (U-Pb zircon) [*Hanmer et al.*, 1994]. Recent work on the Godfrey granite, adjacent to the Upper Deck domain, revealed a minimum crystallization age of 2.61 Ga with evidence for metamorphic overgrowths at circa 2.53–2.51 Ga [*Baldwin et al.*, 2003]. New data presented below provide the first in situ-based constraints on the timing of early subhorizontal fabrics in both the Mary batholith and the EAMT domain of the Athabasca granulite terrane, in addition to timing the age of overprinting D_2 structures. Multiple grains of monazite were identified in thin section, but only grains that could be texturally and compositionally linked to synkinematic and/or synmetamorphic growth during S_1 or S_2 strain were selected for dating (e.g., Figures 14–16 and Table 2). Details regarding in situ trace element analysis and Th-U-total Pb dating of monazite by EPMA are summarized in Appendix A and by *Dumond et al.* [2008]. Monazite dates are depicted as a single Gaussian probability distribution for each monazite compositional domain (Figures 15 and 17). Multiple domains from one or more grains (interpreted to represent the same monazite growth event based on similarity in date, composition, and/or texture) are grouped together using a weighted mean age with 2σ uncertainty. Results from a "consistency" standard of known age are presented to document short-term systematic error and provide a qualitative assessment of accuracy during each analytical session [*Williams et al.*, 2006]. All results are plotted as histograms scaled relative to the consistency standard (e.g., Figures 15 and 17). The standard used in this study is the Moacyr Brazilian pegmatite monazite with weighted mean ages of 506 ± 1 (2σ, MSWD = 0.6) for $^{208}Pb/^{232}Th$, 506.7 ± 0.8 Ma (2σ, MSWD = 0.83) for $^{207}Pb/^{235}U$, and 515.2 ± 0.6 Ma (2σ, MSWD = 0.36) for $^{206}Pb/^{238}U$ obtained by ID-TIMS at the Geological Survey of Canada (W. J. Davis, personal communication, 2006).

6.1. Linking Monazite Geochronology to S_1 Strain and Synkinematic Garnet Growth

[37] Dated samples come from infolded sheets of garnet-rich felsic granulite (tens of m in thickness) that are associated with orthogneisses of the Mary batholith. The sheets occur in both low- and high-D_2 strain domains (samples 04G-067 and 04G-050B, respectively, in Figures 4b, 4d, and 5a). Garnet-rich felsic granulites in domain 3 of the transect contain the penetrative mylonitic S_1 gneissic fabric with top-to-the-SE kinematics (sample 04G-067 in Figures 5a and 14). The main assemblage defining the S_1 fabric includes garnet + K-feldspar + plagioclase + quartz. Rare inclusions of biotite occur in garnet. Garnet locally occurs in the recrystallized mantle of plagioclase porphyroclasts (Figure 14), similar in context to garnet in the granodioritic orthog-

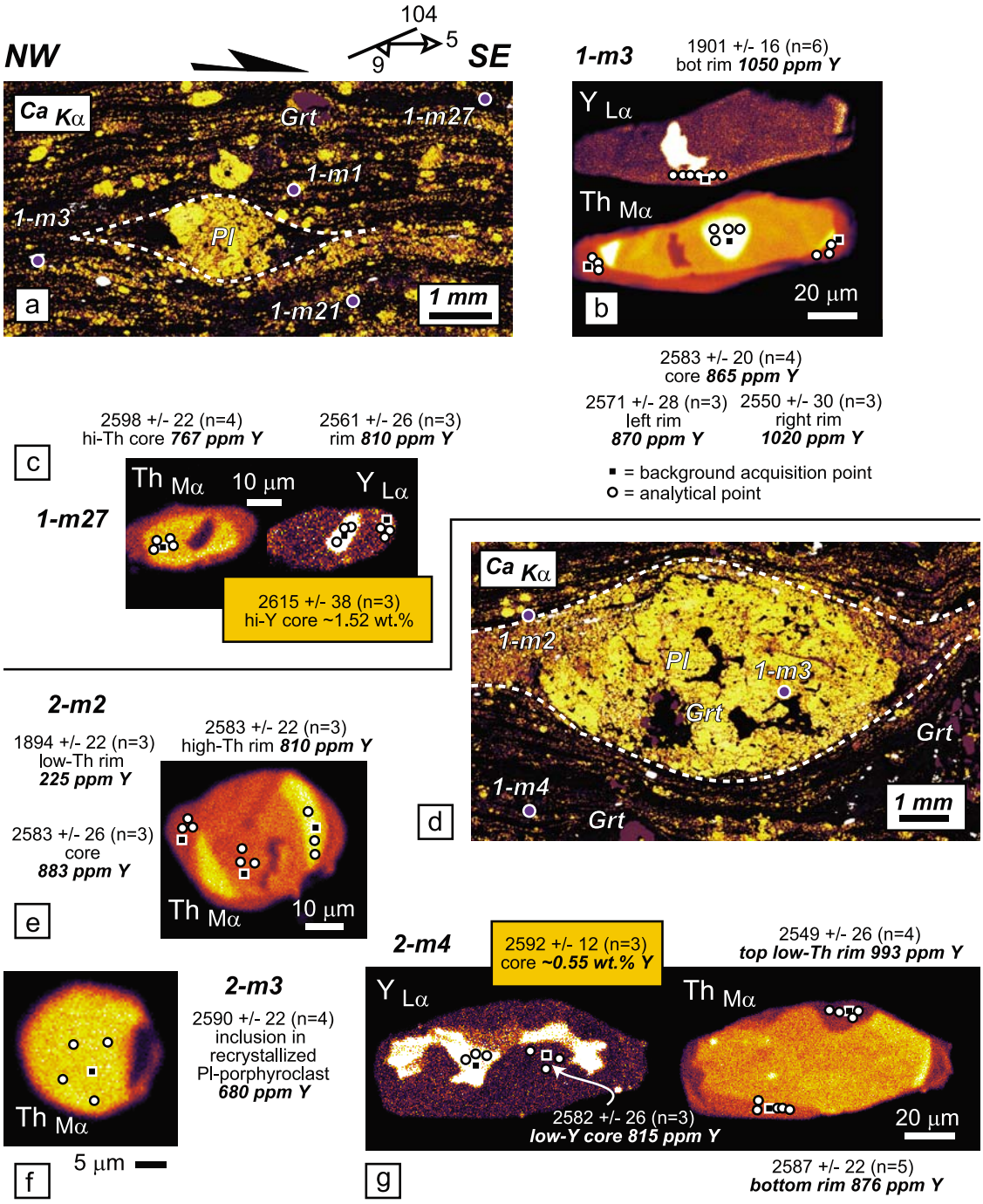

Figure 14. (a and d) X-ray maps of plagioclase porphyroclasts in garnet-bearing S_1 felsic granulite migmatite. Note locations of analyzed monazite grains. In Figure 14d, note garnet in recrystallized mantle of porphyroclast. (b, c, e, f, and g) Maps and EPMA data for a representative set of grains are illustrated for comparison. Note resorbed high-Y cores and low-Y, high-Th overgrowths. Some overgrowths display stair stepping or sigmoidal geometries consistent with top-to-the-SE kinematics (e.g., high-Th zones in Figure 14b, 1-m3, and Figure 14e, 2-m2). Dates are reported at 95% confidence. See Table 2 for summary of data for all eight analyzed grains, i.e., sample 04G-067.

neisses discussed in sections 4 and 5 (e.g., Figures 12a and 13). Garnet more commonly appears as large (up to 2–3 cm) isolated porphyroblasts in the matrix with plagioclase and K-feldspar. K-feldspar clasts, quartz ribbons, and tails of plagioclase clasts all display microstructural evidence for buckling and reactivation of the S_1 gneissic fabric during D_2, as observed around garnet porphyroblasts in outcrop (Figure 11c). In all samples, biotite ± muscovite appear as

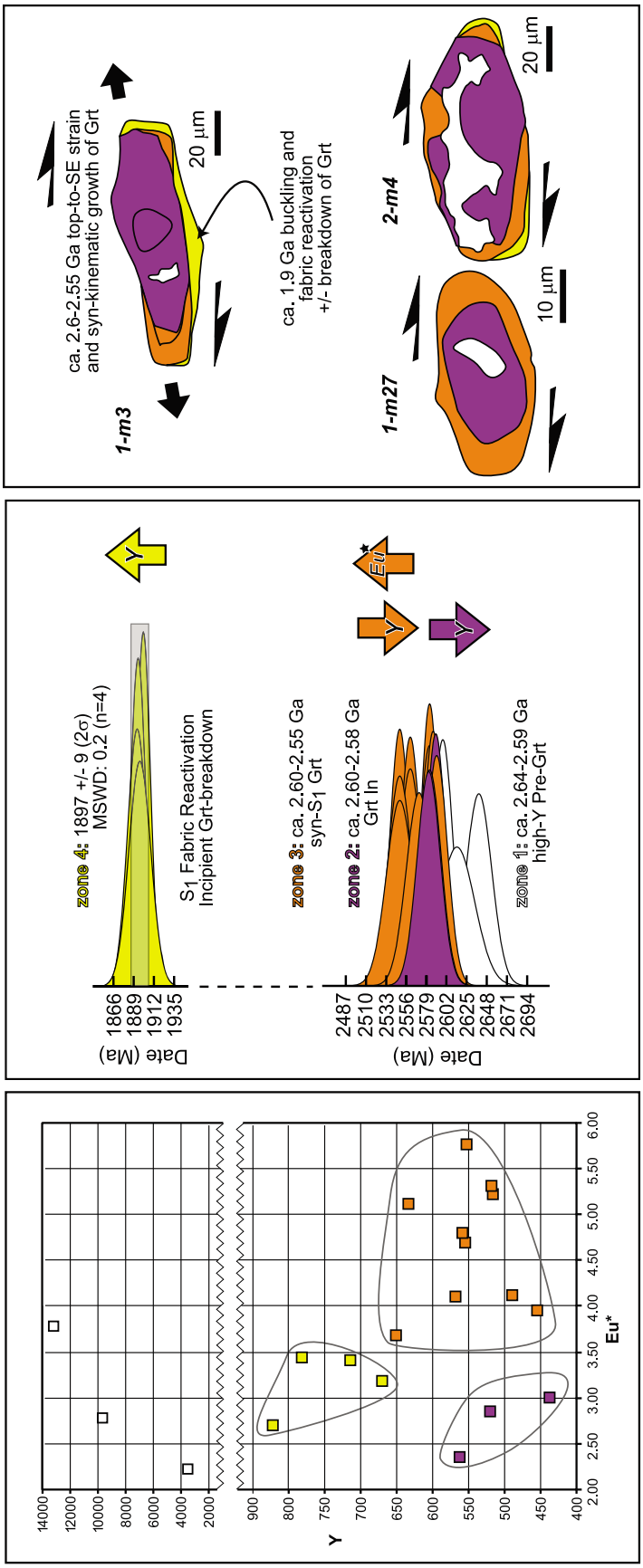

Figure 15. (middle and right) Summary of EPMA monazite data for garnet-bearing S_1 felsic granulite migmatites (see Table 2). (left) Normalized relative to chondrite using the values of *McDonough and Sun* [1995]. See text for discussion.

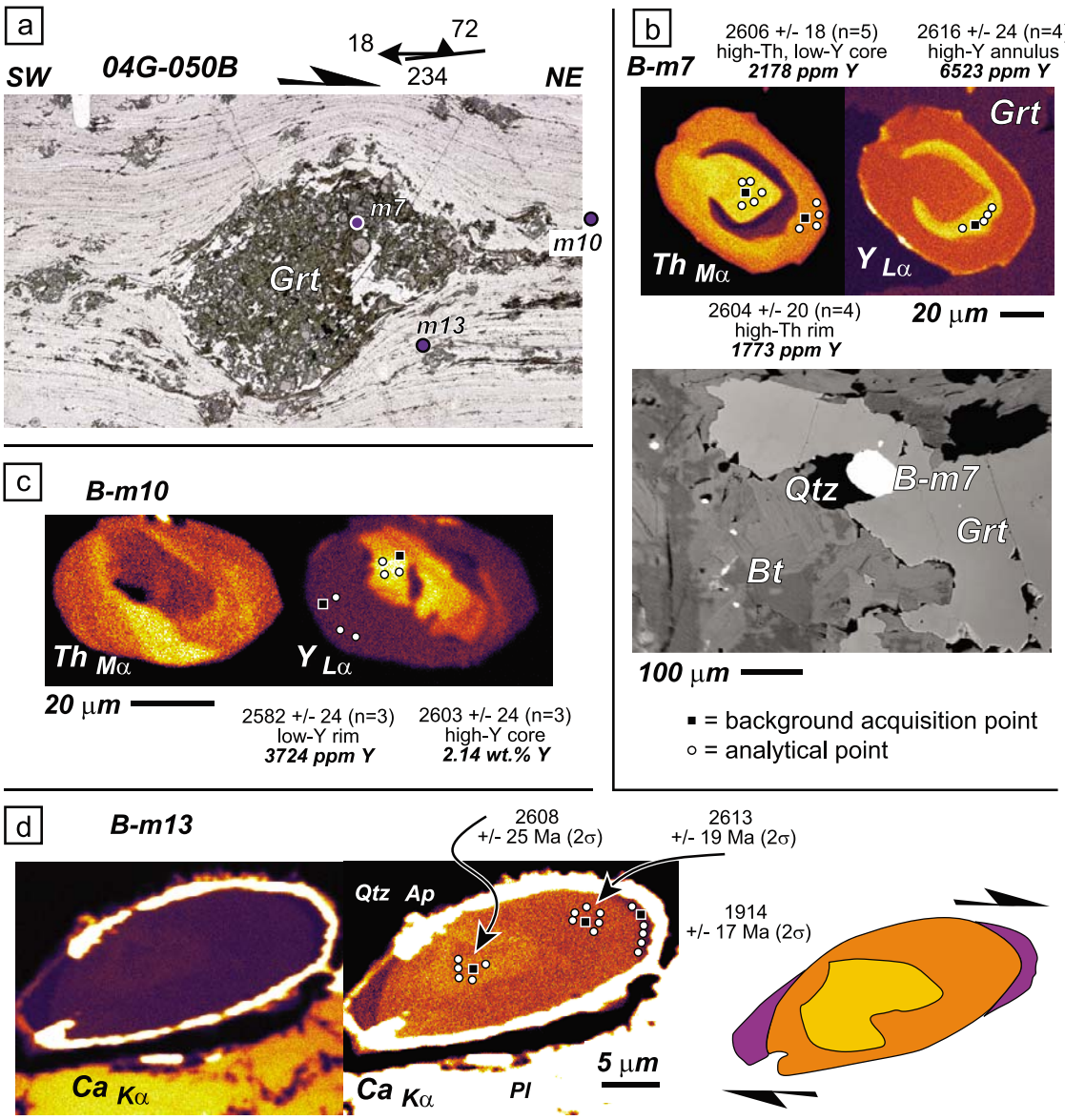

Figure 16. (a) High-resolution thin section scan of garnet-bearing S_2 felsic granulite ultramylonite with location of representative grains illustrated in the figure. (b) X-ray maps and BSE image of monazite grain B-m7 included in garnet. Note high-Th overgrowth cutting across high-Y annulus. (c) Matrix grain B-m10 with resorbed high-Y core and Neoarchean low-Y overgrowth supporting Neoarchean growth of garnet. Note lack of evidence for Paleoproterozoic monazite despite its occurrence in the matrix. (d) Matrix grain B-m13 with synkinematic low-Ca overgrowths associated with apatite indicating dissolution and reprecipitation of monazite during circa 1.9 Ga dextral, top-to-the-NE strain. See Table 2 for summary of data for all 13 analyzed grains in sample 04G-050B.

foliated to randomly oriented mats texturally after garnet. Minor inclusions of biotite in garnet and textural evidence for recrystallization of plagioclase supports the interpretation of the leucocratic sheets as syn-S_1 migmatites produced by a fluid-absent melt reaction, such as [e.g., *Vielzeuf and Montel*, 1994]

$$\text{biotite} + \text{plagioclase} + \text{quartz} \rightarrow \text{garnet} + \text{K-feldspar} + \text{melt}.$$

[38] Microstructural observations demonstrate that garnet grew during S_1 strain at the expense of recrystallized plagioclase (Figures 12a, 13, and 14). Therefore, we use monazite to time garnet growth and hence, S_1 strain and melt production. The petrogenesis of monazite + garnet is commonly inferred from yttrium (Y) zoning in monazite, in the absence of other Y-bearing phases [*Foster et al.*, 2002, 2004; *Gibson et al.*, 2004; *Kelly et al.*, 2006; *Kohn et al.*, 2005; *Mahan et al.*, 2006a; *Pyle et al.*, 2001; *Pyle and*

Table 2. EPMA Monazite Data for Samples 04G-067 and 04G-050B[a]

		Element (wt % Oxide)															
Sample	Domain	CaO	SiO_2	P_2O_5	As_2O_3	La_2O_3	Ce_2O_3	Nd_2O_3	Pr_2O_3	Sm_2O_3	Eu_2O_3	Gd_2O_3	Y_2O_3	ThO_2	UO_2	PbO	Total
04G-067	1-m1 core	0.97	0.98	27.80	0.14	13.90	28.55	11.41	2.83	0.47	0.73	0.62	0.11	7.21	0.20	1.04	96.96
04G-067	1-m1 rim	0.85	0.71	28.75	0.14	14.20	29.07	12.19	2.93	0.86	0.77	0.87	0.16	5.53	0.30	0.63	97.95
04G-067	1-m3 hi-Th core	1.33	1.50	27.49	0.35	12.94	27.08	10.74	2.63	0.33	0.67	0.37	0.11	10.37	0.10	1.42	97.44
04G-067	1-m3 Rt rim	0.82	0.61	29.10	0.23	14.48	30.37	12.11	2.96	0.49	0.75	0.78	0.13	4.64	0.26	0.73	98.46
04G-067	1-m3 Lt rim	0.85	0.75	29.23	0.24	14.20	30.17	11.95	2.95	0.48	0.77	0.52	0.11	5.20	0.27	0.82	98.50
04G-067	1-m3 bot rim	0.84	0.72	28.76	bd	14.36	29.46	11.95	2.97	0.59	0.78	0.95	0.13	5.17	0.34	0.61	97.65
04G-067	1-m20 hi-Y core	0.47	0.14	30.28	0.20	15.55	31.58	9.96	2.95	0.43	0.71	0.77	2.63	0.95	0.86	0.58	98.05
04G-067	1-m21 core	0.98	1.14	28.19	0.21	14.02	28.83	11.20	2.93	0.49	0.71	0.60	0.09	7.53	0.21	1.09	98.20
04G-067	1-m21 rim	0.76	0.52	29.30	bd	14.93	30.47	12.18	2.97	0.63	0.79	0.79	0.14	4.06	0.34	0.50	98.39
04G-067	1-m27 hi-Y core	0.46	0.25	29.53	0.25	14.83	30.69	11.48	2.98	0.65	0.79	1.16	1.92	1.47	0.43	0.42	97.29
04G-067	1-m27 hi-Th core	0.98	1.09	28.03	0.34	13.90	28.66	11.32	2.82	0.42	0.70	0.63	0.10	7.08	0.21	1.05	97.32
04G-067	1-m27 rim	0.97	1.11	27.72	0.20	13.77	28.63	11.40	2.91	0.48	0.74	0.39	0.10	7.30	0.23	1.07	97.04
04G-067	2-m2 core	1.20	0.66	29.09	0.22	14.23	28.97	11.64	2.98	0.88	0.73	1.02	0.11	6.57	0.38	1.06	99.74
04G-067	2-m2 NE hi-Th rim	1.28	1.83	26.75	0.51	12.50	26.84	10.80	2.77	0.35	0.72	0.48	0.10	10.78	0.20	1.53	97.44
04G-067	2-m2 NW rim	0.85	0.87	27.88	0.16	14.52	28.95	11.38	2.85	0.63	0.74	0.68	0.16	5.74	0.35	0.66	96.41
04G-067	2-m3 core	1.27	0.83	28.31	0.31	13.79	28.32	11.29	2.92	0.56	0.69	0.88	0.09	6.79	0.41	1.10	97.55
04G-067	2-m4 hi-Y core	1.43	0.61	29.51	0.29	13.64	27.74	10.97	2.70	0.75	0.68	1.14	0.70	6.99	0.58	1.22	98.96
04G-067	2-m4 lo-Y core	1.15	0.78	28.26	0.15	13.39	28.29	11.62	2.92	0.80	0.70	0.69	0.10	6.72	0.28	1.03	96.87
04G-067	2-m4 bot	0.84	0.80	28.94	0.28	14.47	30.54	11.65	2.90	0.42	0.73	0.52	0.11	5.48	0.25	0.85	98.78
04G-067	2-m4 top	0.72	0.52	29.24	0.53	15.41	31.60	12.00	3.14	0.40	0.77	0.53	0.13	4.18	0.26	0.67	100.10
04G-050B	B-m1 NE rim	0.80	1.16	29.32	bd	14.43	28.89	11.55	2.90	0.81	0.67	0.95	0.31	6.32	0.41	0.74	99.33
04G-050B	B-m1 NW core	1.13	1.18	28.87	0.33	11.98	25.65	11.12	2.81	1.10	0.65	1.58	1.79	7.93	0.54	1.32	97.99
04G-050B	B-m3 core	0.97	0.23	30.44	0.36	12.00	28.78	12.90	3.18	1.29	0.76	1.63	0.83	3.92	0.47	0.76	98.52
04G-050B	B-m3 rim	1.30	0.75	29.61	0.36	12.26	27.36	12.25	3.05	0.99	0.72	1.16	0.36	7.31	0.28	1.10	98.85
04G-050B	B-m4 rim	1.27	0.71	29.44	0.28	11.73	27.84	12.95	3.15	0.84	0.76	1.04	0.20	6.52	0.71	1.22	98.66
04G-050B	B-m5 core	1.32	0.77	29.58	0.24	11.95	26.94	12.20	3.01	1.02	0.69	1.39	0.34	7.53	0.29	1.15	98.42
04G-050B	B-m7 hi-Y ring	0.92	0.24	30.05	0.22	12.04	29.11	12.90	3.23	1.15	0.76	1.54	0.83	3.63	0.48	0.73	97.82
04G-050B	B-m7 core	1.42	0.95	29.08	0.41	11.72	26.75	12.18	3.07	0.70	0.70	1.01	0.28	8.53	0.31	1.30	98.38
04G-050B	B-m7 rim	1.23	0.86	29.17	bd	11.97	27.65	12.72	3.14	0.82	0.73	0.87	0.23	6.85	0.61	1.23	98.12
04G-050B	B-m9 core	1.14	1.35	29.13	0.47	11.62	26.74	12.67	2.93	1.03	0.72	1.31	0.55	8.55	0.29	1.28	99.76
04G-050B	B-m10 core	1.28	0.58	30.82	0.20	12.71	26.43	11.19	2.71	0.89	0.66	1.48	2.72	6.01	0.73	1.17	99.59
04G-050B	B-m10 rim	1.16	0.95	29.32	0.17	12.46	27.16	11.78	3.08	0.87	0.72	1.14	0.47	7.38	0.36	1.16	98.18
04G-050B	B-m11 mid core	1.84	1.33	28.50	0.44	11.05	24.52	10.82	2.82	0.89	0.65	1.12	0.39	11.66	0.38	1.69	98.09
04G-050B	B-m11 Rt tip	1.10	1.25	28.39	0.15	12.30	26.97	11.58	2.89	1.00	0.69	0.98	0.30	8.36	0.40	0.93	97.29
04G-050B	B-m13 core	1.59	0.57	29.50	0.61	10.77	25.71	12.66	2.92	1.44	0.71	2.03	0.97	8.03	0.39	1.27	99.19
04G-050B	B-m13 outer core	1.49	0.79	29.98	0.42	11.56	26.47	12.43	2.89	1.28	0.65	1.49	0.66	8.10	0.37	1.27	99.84
04G-050B	B-m13 rim	1.06	1.58	29.21	0.28	12.25	27.82	12.77	3.08	1.23	0.75	1.38	0.48	8.27	0.36	0.92	101.45
04G-050B	B-m14 core	1.72	0.81	29.35	0.38	10.90	25.20	12.12	2.87	1.34	0.68	1.78	0.93	9.40	0.42	1.43	99.32
04G-050B	B-m15 core	1.54	2.19	27.35	0.46	10.30	24.85	11.82	2.81	0.61	0.69	1.10	0.30	13.27	0.40	1.97	99.64
04G-050B	B-m15 SW tip	0.85	1.19	28.92	bd	14.03	28.75	11.46	2.91	0.72	0.68	0.88	0.22	6.88	0.38	0.78	98.74
04G-050B	B-m16 core	1.31	0.78	29.84	0.41	11.95	27.27	12.44	3.01	1.13	0.71	1.67	0.53	7.52	0.33	1.18	100.09
04G-050B	B-m18 core2	1.35	0.82	30.30	0.35	12.37	27.57	12.64	3.01	1.09	0.72	1.20	0.40	7.56	0.30	1.15	100.84
04G-050B	B-m18 top rim	1.21	1.60	29.31	0.34	11.43	27.40	12.89	3.06	0.93	0.74	0.92	0.26	9.14	0.47	1.44	101.15
Moacyr	12/2/2006	0.45	1.26	28.25	0.60	14.24	28.82	11.08	2.98	0.98	0.76	0.88	1.42	6.67	0.08	0.17	98.63
Moacyr	12/3/2006	0.45	1.22	28.03	0.11	14.10	28.81	11.14	2.99	0.98	0.78	0.79	1.43	6.70	0.08	0.17	97.79
Moacyr	12/8/2006	0.44	1.23	28.04	0.02	14.15	28.68	11.01	3.00	1.04	0.75	1.04	1.42	6.67	0.09	0.17	97.77
Moacyr	12/10/2006	0.44	1.36	27.74	0.36	14.21	28.62	11.00	2.87	0.98	0.73	0.91	1.45	6.66	0.09	0.17	97.59
Moacyr	12/12/2006	0.44	1.28	26.53	0.21	13.89	28.47	10.88	2.96	1.00	0.75	0.99	1.45	6.71	0.08	0.17	95.83
Moacyr	12/15/2006	0.47	1.30	28.75	1.39	14.33	28.74	10.97	3.07	0.92	0.75	0.78	1.43	6.76	0.09	0.17	99.91
Moacyr	12/17/2006	0.45	1.28	28.48	0.06	14.20	28.50	10.94	3.06	0.87	0.74	0.83	1.41	6.72	0.09	0.17	97.79
Moacyr	1/20/2007	0.42	1.40	28.49	0.34	14.41	29.04	11.25	3.09	0.88	0.73	1.03	1.40	6.75	0.08	0.17	99.50
Moacyr	1/21/2007	0.42	1.39	27.74	0.21	14.49	29.00	11.19	2.95	0.85	0.74	0.85	1.42	6.79	0.07	0.17	98.27
Moacyr	1/22/2007	0.42	1.43	28.79	0.03	14.49	29.12	11.17	3.02	0.91	0.75	0.69	1.42	6.73	0.08	0.17	99.21
Moacyr	1/25/2007	0.41	1.46	28.73	0.18	14.35	29.29	11.33	3.04	0.87	0.76	1.12	1.39	6.68	0.10	0.17	99.86
Moacyr	1/29/2007	0.42	1.51	28.89	0.38	14.44	29.26	11.44	2.97	0.94	0.75	0.99	1.43	6.66	0.10	0.17	100.36
Moacyr	1/31/2007	0.43	1.41	28.30	0.56	14.39	29.03	11.16	3.02	0.84	0.75	1.10	1.43	6.75	0.08	0.17	99.41

Table 2. (continued)

Cations (per Formula Unit) on the Basis of 4 Oxygens														
Ca	Si	P	As	La	Ce	Nd	Pr	Sm	Eu	Gd	Y	Th	U	Pb
0.043	0.040	0.964	0.003	0.210	0.429	0.167	0.042	0.007	0.010	0.009	0.002	0.072	0.002	0.011
0.037	0.028	0.979	0.003	0.211	0.428	0.175	0.043	0.012	0.010	0.012	0.003	0.054	0.003	0.006
0.058	0.061	0.947	0.009	0.194	0.404	0.156	0.039	0.005	0.009	0.005	0.002	0.102	0.001	0.015
0.035	0.025	0.983	0.005	0.213	0.443	0.173	0.043	0.007	0.010	0.010	0.003	0.045	0.002	0.007
0.036	0.030	0.984	0.006	0.208	0.439	0.170	0.043	0.006	0.010	0.007	0.002	0.050	0.002	0.008
0.037	0.029	0.982	0.001	0.214	0.435	0.173	0.044	0.008	0.011	0.013	0.003	0.051	0.003	0.006
0.020	0.005	1.004	0.005	0.225	0.453	0.139	0.042	0.006	0.010	0.010	0.054	0.009	0.008	0.006
0.042	0.046	0.962	0.005	0.208	0.426	0.161	0.043	0.007	0.010	0.008	0.002	0.074	0.002	0.011
0.032	0.021	0.990	0.000	0.220	0.446	0.174	0.043	0.009	0.011	0.010	0.003	0.040	0.003	0.005
0.020	0.010	0.995	0.006	0.218	0.447	0.163	0.043	0.009	0.011	0.015	0.041	0.014	0.004	0.004
0.042	0.045	0.964	0.009	0.208	0.426	0.164	0.042	0.006	0.010	0.008	0.002	0.070	0.002	0.011
0.043	0.046	0.959	0.005	0.208	0.429	0.167	0.043	0.007	0.010	0.005	0.002	0.072	0.002	0.011
0.051	0.026	0.977	0.005	0.208	0.421	0.165	0.043	0.012	0.010	0.013	0.003	0.063	0.003	0.010
0.056	0.075	0.929	0.013	0.189	0.403	0.158	0.041	0.005	0.010	0.006	0.002	0.107	0.002	0.016
0.038	0.036	0.969	0.004	0.220	0.435	0.167	0.043	0.009	0.010	0.009	0.003	0.057	0.003	0.007
0.055	0.034	0.971	0.008	0.206	0.420	0.163	0.043	0.008	0.010	0.012	0.002	0.067	0.004	0.012
0.060	0.024	0.986	0.007	0.198	0.401	0.155	0.039	0.010	0.009	0.015	0.015	0.067	0.005	0.012
0.050	0.032	0.976	0.003	0.201	0.422	0.169	0.043	0.011	0.010	0.009	0.002	0.066	0.003	0.011
0.036	0.032	0.977	0.007	0.213	0.446	0.166	0.042	0.006	0.010	0.007	0.002	0.053	0.002	0.008
0.031	0.021	0.977	0.013	0.224	0.457	0.169	0.045	0.006	0.011	0.007	0.003	0.040	0.002	0.007
0.034	0.046	0.979	0.002	0.210	0.417	0.163	0.042	0.011	0.009	0.013	0.006	0.061	0.004	0.007
0.048	0.047	0.970	0.008	0.175	0.373	0.158	0.041	0.015	0.009	0.021	0.038	0.076	0.005	0.013
0.041	0.009	1.010	0.009	0.174	0.413	0.181	0.045	0.017	0.010	0.021	0.017	0.037	0.004	0.008
0.055	0.029	0.989	0.009	0.178	0.395	0.173	0.044	0.013	0.010	0.015	0.008	0.070	0.002	0.011
0.054	0.028	0.990	0.007	0.172	0.405	0.184	0.046	0.011	0.010	0.014	0.004	0.063	0.006	0.012
0.056	0.031	0.990	0.006	0.174	0.390	0.172	0.043	0.014	0.009	0.018	0.007	0.072	0.003	0.011
0.039	0.010	1.007	0.006	0.176	0.422	0.183	0.047	0.016	0.011	0.020	0.018	0.035	0.004	0.007
0.061	0.038	0.979	0.010	0.172	0.390	0.173	0.044	0.010	0.009	0.013	0.006	0.082	0.003	0.013
0.053	0.035	0.987	0.001	0.177	0.405	0.182	0.046	0.011	0.010	0.012	0.005	0.066	0.005	0.012
0.048	0.053	0.967	0.011	0.168	0.384	0.177	0.042	0.014	0.010	0.017	0.011	0.081	0.002	0.013
0.053	0.022	0.999	0.004	0.179	0.371	0.153	0.038	0.012	0.009	0.019	0.055	0.056	0.006	0.011
0.049	0.038	0.985	0.004	0.182	0.394	0.167	0.044	0.012	0.010	0.015	0.010	0.071	0.003	0.011
0.079	0.053	0.966	0.011	0.163	0.359	0.155	0.041	0.012	0.009	0.015	0.008	0.113	0.003	0.017
0.048	0.050	0.970	0.004	0.183	0.399	0.167	0.043	0.014	0.009	0.013	0.007	0.082	0.004	0.009
0.067	0.023	0.985	0.015	0.157	0.371	0.178	0.042	0.020	0.010	0.027	0.020	0.077	0.003	0.013
0.062	0.031	0.988	0.010	0.166	0.377	0.173	0.041	0.017	0.009	0.019	0.014	0.077	0.003	0.013
0.044	0.061	0.958	0.006	0.175	0.395	0.177	0.044	0.016	0.010	0.018	0.010	0.077	0.003	0.009
0.073	0.032	0.979	0.009	0.158	0.364	0.170	0.041	0.018	0.009	0.023	0.020	0.090	0.004	0.014
0.066	0.088	0.927	0.011	0.152	0.364	0.169	0.041	0.008	0.009	0.015	0.007	0.129	0.003	0.020
0.036	0.048	0.974	0.002	0.206	0.419	0.163	0.042	0.010	0.009	0.011	0.005	0.066	0.003	0.008
0.055	0.031	0.986	0.010	0.172	0.390	0.173	0.043	0.015	0.009	0.021	0.011	0.071	0.003	0.012
0.056	0.032	0.990	0.008	0.176	0.390	0.174	0.042	0.014	0.010	0.015	0.008	0.071	0.003	0.011
0.050	0.062	0.963	0.008	0.163	0.389	0.179	0.043	0.012	0.010	0.012	0.005	0.086	0.004	0.014
0.019	0.050	0.953	0.014	0.209	0.420	0.158	0.043	0.013	0.010	0.012	0.030	0.064	0.001	0.002
0.020	0.049	0.956	0.003	0.210	0.425	0.160	0.044	0.013	0.011	0.010	0.031	0.066	0.001	0.002
0.019	0.049	0.956	0.000	0.210	0.423	0.159	0.044	0.014	0.010	0.014	0.031	0.065	0.001	0.002
0.019	0.055	0.948	0.009	0.211	0.423	0.159	0.043	0.014	0.010	0.012	0.031	0.065	0.001	0.002
0.020	0.054	0.935	0.005	0.213	0.434	0.162	0.045	0.014	0.011	0.014	0.032	0.068	0.001	0.002
0.020	0.051	0.952	0.033	0.207	0.412	0.153	0.044	0.012	0.010	0.010	0.030	0.064	0.001	0.002
0.020	0.051	0.963	0.002	0.209	0.417	0.156	0.045	0.012	0.010	0.011	0.030	0.065	0.001	0.002
0.018	0.055	0.952	0.008	0.210	0.420	0.159	0.044	0.012	0.010	0.013	0.030	0.065	0.001	0.002
0.018	0.056	0.946	0.005	0.215	0.427	0.161	0.043	0.012	0.010	0.011	0.031	0.066	0.001	0.002
0.018	0.057	0.962	0.001	0.211	0.421	0.158	0.044	0.012	0.010	0.009	0.030	0.064	0.001	0.002
0.017	0.058	0.956	0.004	0.208	0.421	0.159	0.044	0.012	0.010	0.015	0.029	0.064	0.001	0.002
0.018	0.059	0.954	0.009	0.208	0.418	0.159	0.042	0.013	0.010	0.013	0.030	0.063	0.001	0.002
0.018	0.056	0.949	0.013	0.210	0.421	0.158	0.043	0.011	0.010	0.015	0.030	0.065	0.001	0.002

Table 2. (continued)

	Y[b]		Th		U		Pb			
Cation Sum	WtAv	2σBk	WtAv	2σBk	WtAv	2σBk	WtAv	2σBk	Date With 2σ bkg	n
1.049	890	48	67415	290	1747	42	9028	32	2561 ± 23	4 of 5
1.033	1289	44	51540	204	2641	46	5412	20	1894 ± 17	5 of 5
1.067	865	48	97016	408	920	26	12322	40	2583 ± 20	4 of 4
1.031	1018	56	43297	224	2292	58	6343	30	2550 ± 30	3 of 4
1.028	869	54	48135	248	2391	56	7065	32	2571 ± 29	3 of 4
1.032	1050	40	48370	176	3037	44	5288	18	1901 ± 16	6 of 6
1.002	20062	140	8242	64	6569	68	4389	22	2639 ± 28	3 of 4
1.050	712	46	70457	302	1842	42	9396	32	2550 ± 22	4 of 4
1.022	1119	58	37992	202	3016	64	4341	24	1896 ± 25	3 of 6
1.017	14885	136	13587	94	3403	70	3538	22	2615 ± 41	3 of 3
1.053	767	48	66110	284	1823	42	9048	32	2598 ± 23	4 of 4
1.059	810	54	68274	338	1989	50	9248	38	2561 ± 26	3 of 3
1.041	858	56	61336	306	3383	60	9188	38	2583 ± 26	3 of 5
1.091	811	62	100815	488	1750	42	13205	50	2583 ± 23	3 of 5
1.047	1226	64	53525	272	3041	60	5713	28	1894 ± 22	3 of 6
1.049	680	52	63391	274	3493	52	9532	34	2590 ± 22	4 of 4
1.024	5500	84	654111	326	5155	68	10598	42	2592 ± 24	3 of 4
1.039	814	62	62896	314	2440	54	8903	36	2582 ± 26	3 of 5
1.035	876	42	51203	202	2201	44	7369	24	2587 ± 22	5 of 5
1.044	993	48	39094	178	2310	50	5840	24	2549 ± 27	4 of 5
1.025	2416	64	59075	258	3621	27	6439	26	1907 ± 18	4 of 6
1.038	14102	102	74172	258	4790	46	11473	32	2588 ± 17	6 of 6
1.003	6531	66	36565	128	4115	44	6556	20	2597 ± 20	7 of 7
1.030	2854	60	68346	262	2432	42	9570	30	2584 ± 20	5 of 5
1.046	1576	66	60980	306	6247	72	10556	42	2582 ± 24	3 of 6
1.054	2687	76	70343	348	2554	54	9953	40	2602 ± 26	3 of 4
1.003	6511	86	33911	158	4226	58	6348	26	2616 ± 26	4 of 4
1.032	2176	56	79769	304	2760	42	11241	34	2606 ± 19	5 of 8
1.045	1772	60	64068	276	5396	58	10613	36	2604 ± 21	4 of 5
1.039	4309	86	80010	392	2514	52	11049	42	2587 ± 24	3 of 5
1.005	21222	182	56183	284	6398	72	10147	40	2603 ± 24	3 of 5
1.018	3724	82	69005	342	3190	58	10010	40	2580 ± 26	3 of 5
1.044	3055	76	109119	526	3353	54	14598	54	2519 ± 22	3 of 5
1.037	2380	72	78230	384	3520	58	8064	34	1898 ± 19	3 of 4
1.032	7633	84	75052	286	3418	46	11001	34	2609 ± 19	5 of 5
1.019	5230	64	75757	264	3252	40	11027	30	2614 ± 17	6 of 6
1.051	3804	64	77316	294	3204	44	7950	26	1914 ± 15	5 of 5
1.034	7306	82	87905	332	3664	44	12432	36	2559 ± 18	5 of 6
1.087	2374	56	124053	460	3455	42	17026	48	2599 ± 17	5 of 7
1.033	1754	52	64306	248	3336	46	6789	24	1901 ± 16	5 of 6
1.030	4155	60	70381	246	2951	40	10219	28	2616 ± 18	6 of 6
1.015	3135	60	70748	272	2668	42	9921	30	2570 ± 10	5 of 5
1.046	2079	54	85530	324	4164	48	12473	36	2573 ± 18	5 of 5
1.056	11208	90	62393	242	690	24	1455	12	501 ± 7	5 of 5
1.051	11264	102	62688	272	685	28	1467	14	502 ± 8	4 of 4
1.051	11218	90	62433	242	762	26	1477	12	506 ± 7	5 of 5
1.062	11383	112	62298	270	822	30	1453	14	498 ± 8	4 of 4
1.083	11395	100	62780	242	729	26	1465	12	500 ± 7	5 of 5
1.057	11289	110	63260	274	791	30	1507	14	509 ± 8	4 of 4
1.038	11111	110	62883	272	769	30	1483	14	505 ± 8	4 of 4
1.054	11056	186	63128	244	680	24	1490	12	507 ± 6	5 of 5
1.064	11211	128	63474	316	646	30	1472	16	500 ± 8	3 of 3
1.041	11165	110	62952	272	696	28	1487	14	507 ± 8	4 of 4
1.048	10970	90	62483	220	907	26	1513	12	514 ± 6	6 of 6
1.051	11251	112	62340	270	844	30	1488	14	508 ± 8	4 of 4
1.060	11230	78	63160	192	723	20	1471	10	500 ± 6	8 of 8

[a]Tb, Dy, Ho, Er, and Yb were analyzed and found below detection (bd, below detection); Sample 04G-067location: UTM E 398477 N 6576399 zone 13V NAD 27; and sample 04G-050B location: UTM E 394608 N 6576821 zone 13V NAD 27. WtAv, weighted average; 2σBk, 2-sigma uncertainty with background error included; bkg, background.

[b]With the exception of Y, Th, U, and Pb, all elements are reported as simple means. Values for Y, Th, U, and Pb are reported as weighted means with the error based on propagation of the standard deviation of the mean of the X-ray counting uncertainties (for n analyses) plus 1% uncertainty on the estimated background intensities through the age equation [*Williams et al.,* 2006].

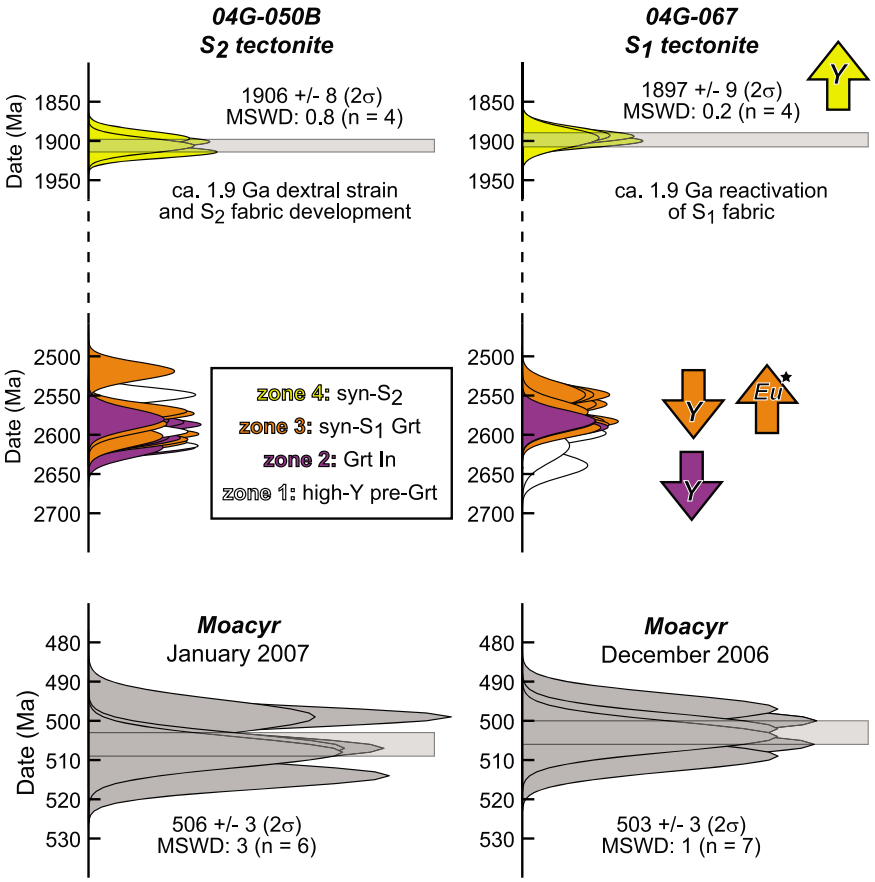

Figure 17. Annotated monazite histogram summary comparing dates for samples 04G-067 and 04G-050B with Moacyr consistency standard for reference. Color scheme for monazite zones is same as in Figure 15. See Table 2 for summary of all data.

Spear, 2003; *Zhu and O'Nions*, 1999]. Monazite is a light rare earth element (LREE)-rich phosphate that is depleted in Y and heavy rare earth elements (HREEs) when it precipitates during or after growth of garnet, a phase that readily incorporates Y and HREEs [e.g., *Zhu and O'Nions*, 1999]. In the case of the fluid-absent melt reaction proposed for the S_1 migmatites, the following petrogenesis would be anticipated:

$$\text{high-Y monazite}_1 + \text{biotite} + \text{plagioclase} + \text{quartz} \rightarrow \text{low-Y monazite}_2 + \text{garnet} + \text{K-feldspar} + \text{melt}.$$

[39] In addition to Y, the Eu content and the Eu anomaly for each monazite domain are useful for quantifying depletions (or enrichments) of Sm + Gd due to contemporaneous growth (or breakdown) of garnet. Eight monazite grains were analyzed in situ via EPMA in the matrix near δ-type plagioclase porphyroclasts in 04G-067 (Figures 14 and 15 and Table 2). Four zones were identified by combining high-resolution X-ray maps of Y (Figure 14) with a chondrite-normalized plot of Y versus Eu*, where Eu* represents the Eu anomaly for each analyzed domain (Figure 15). Zone 1 is defined by high-Y resorbed cores (0.55–2.07 wt %) with relatively low Eu anomalies (Eu* < 4.00) and dated at circa 2.64–2.59 Ga (see monazite 1-m3, 1-m27, and 2-m2 in Figures 14 and 15). Zones 2 and 3 correspond to low-Y overgrowths (0.07–0.10 wt %) (see monazite 1-m3, 1-m27, and 2-m4 in Figures 14 and 15). Zone 2 and 3 monazites locally display stair stepping and σ-type geometries consistent with top-to-the-ESE kinematics (e.g., as defined by Th in X-ray maps for grains 1-m3, 1-m27, and 2-m2 in Figures 14 and 15). The distinction between zones 2 and 3 is based on the Eu anomaly, with zone 3 displaying the most positive Eu anomalies (Eu* < 3.50 in Figure 15) attributed to depletions of Sm + Gd and HREEs relative to Eu. Zones 2 and 3 have been dated at circa 2.60–2.55 Ga (Figure 15). Zone 4 coincides with thin (<10 μm) irregular rims dated at circa 1.9 Ga that are slightly enriched in Y (0.10–1.3 wt %) relative to zones 2 and 3 (e.g., see monazite 1-m3 in Figures 14 and 15).

[40] The sharp transition from high-Y zone 1 to low-Y zones 2 and 3 monazite is most consistent with the onset of garnet growth, dated at circa 2.6–2.55 Ga (Figure 15). Garnet growth is also supported by the observation that zone 3 monazite domains display the most positive Eu anomalies, i.e., (Table 2 and Figure 15). Dates for zone 2

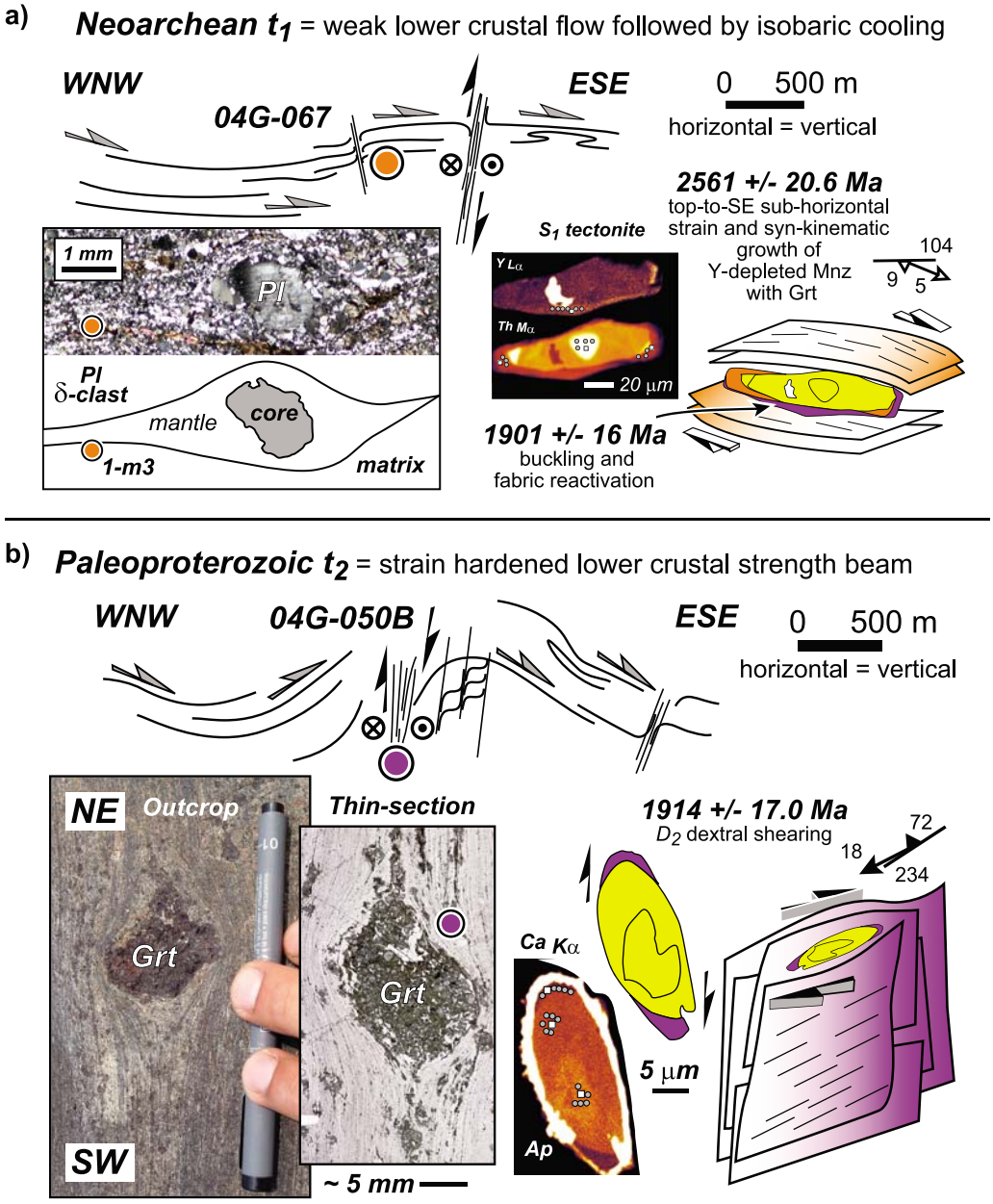

Figure 18. (a) Illustration of penetrative subhorizontal fabric development and Neoarchean lower crustal flow from transect in Figure 4 with example of microstructural and monazite constraints provided by this study. (b) Illustration of steep fabric development, buckling, and folding from a different segment of the transect in Figure 4 emphasizing evidence for a strong lower crust in the Paleoproterozoic with discrete shear zones and nonpenetrative strain at the scale of the transect.

and 3 synkinematic overgrowths provide a direct constraint on the age of top-to-the-SE subhorizontal flow and S_1 strain at circa 2.6–2.55 Ga (Figures 15 and 18). Finally, zone 4 rims display subtle increases in Y that may be due to incipient garnet breakdown [e.g., *Foster et al.*, 2002; *Mahan et al.*, 2006a; *Williams et al.*, 2007], and their presence provides direct evidence for reactivation of the Neoarchean S_1 fabric in the Paleoproterozoic which we infer at 1897 ± 9 Ma (2σ, MSWD = 0.2, n = 4) (Figures 15 and 17).

6.2. Timing Dextral S_2 Strain With Synkinematic Monazite

[41] Ultramylonitic sheets of felsic granulite occur in the NW limb of a map-scale antiform where S_2 strain is localized into a tens of meters wide NE striking, steeply NW dipping dextral shear zone. The dated sample 04G-050B in this shear zone is located in the Mary batholith domain 2 (Figures 4a and 5a). Gneissic S_1 fabrics progressively steepen into the zone marked by complete transpo-

sition of the SE trending L_1 lineation into a gently SW plunging L_2 lineation with dextral, top-to-the-NE kinematics defined by sigmoidal garnet porphyroblasts (up to 4 cm in diameter) (Figures 5a, 11e, and 16).

[42] Garnet in sample 04G-050B is variably retrogressed to biotite. Thirteen monazite grains were analyzed in a large σ-type garnet porphyroclast and in the ultramylonitic matrix via EPMA (Figures 11e and 16 and Table 2). Sealed inclusions in garnet were dated between circa 2.62 Ga and 2.58 Ga (Figure 16b and Table 2). High-Y monazite cores (0.65–2.14 wt %) in both garnet and the matrix yielded dates between circa 2.62 and 2.56 Ga (e.g., grains m7 and m10 in Figure 16 and Table 2). Low-Y monazite overgrowths (1578–7580 ppm) were also identified in garnet and the matrix (e.g., grains m7 and m10 in Figure 16) and dated at circa 2.61–2.57 Ga. Sigmoidal and stair-stepping low-Ca monazite overgrowths are abundant throughout the matrix and display the same D_2 top-to-the-NE kinematics observed around garnet (e.g., grain m13 in Figure 16d). The synkinematic low-Ca monazite overgrowths are dated at 1.91–1.89 Ga (Figures 16d and 17 and Table 2).

[43] The record of Y depletion observed in monazite from sample 04G-050B is consistent with Neoarchean growth of garnet at circa 2.61–2.57 Ga and in agreement with the D_1 synkinematic garnet growth inferred for sample 04G-067 located in the low-D_2 strain domain (Figure 17). Synkinematic low-Ca monazite overgrowths constrain the age of dextral shearing and subvertical fabric development to 1906 ± 8 Ma (2σ, MSWD = 0.8, n = 4) (Figure 17). This age is coincident with the timing of S_1 fabric reactivation documented in sample 04G-067 (Figures 17 and 18).

7. Discussion

[44] Redistribution of mass and heat, evolution of surface topography, and lithospheric-scale strain partitioning/localization are all directly related to the rheological and petrogenetic evolution of continental lower crust during collisional and extensional orogenesis, e.g., the Himalayan-Tibetan system (as reviewed by *Hodges* [2006]) and the Basin and Range of western North America [*Kruse et al.*, 1991; *Wernicke et al.*, 2008]. The important control that rheology of continental lower crust exerts on plate tectonic-scale processes is emphasized by the ongoing debate that persists regarding the mechanisms that control the strength of continental lithosphere [e.g., *Axen et al.*, 1998; *Burov and Watts*, 2006; *Butler*, 2006; *Jackson*, 2002; *Klepeis et al.*, 2004; *Thatcher and Pollitz*, 2008]. Deep seismic reflection profiling [*Nelson*, 1991], experimental rock mechanics [*Rutter and Brodie*, 1992], and recent thermal-mechanical models [*Beaumont et al.*, 2004] can be difficult to reconcile given the dramatic lithological heterogeneity and anisotropy observed in exposed sections of continental lower crust [e.g., *Percival*, 1992]. High-temperature ductile flow of low-viscosity material or the production of a laterally extensive subhorizontal tectonite fabric, however, remain as some of the most feasible mechanisms for explaining the strong seismic anisotropy observed in the lower crust of orogens worldwide [*Meissner et al.*, 2006; *Ross et al.*, 2004].

[45] The long residence time of the Athabasca granulite terrane at lower crustal levels provides an opportunity to examine the behavior of continental lower crust from Archean stabilization to Paleoproterozoic reactivation, uplift, and exhumation [*Flowers et al.*, 2006b, 2008; *Mahan et al.*, 2006a, 2008; *Williams and Hanmer*, 2006]. This record contrasts with exhumed ultrahigh-pressure rocks that experienced a transient response to thickening of continental crust and short-term lower crustal residence, e.g., the >40,000 km^2 Western Gneiss Region in Norway [i.e., *Hacker and Gans*, 2005]. Laterally extensive and nearly intact exposures of continental lower crust, such as described in this study or the Georgian Bay transect [*Culshaw et al.*, 1997], offer some of the best opportunities to explore the deformation mechanisms that attend lower crustal flow [*Hodges*, 2006].

7.1. Subhorizontal Fabrics in Continental Lower Crust: The Mary Batholith Perspective

[46] Subhorizontal S_1 fabrics exposed in the Mary batholith of the Athabasca granulite terrane may represent a field-based analog for the nature of lower crustal flow. This study documents a penetrative, high-temperature (~800°C) ribbon mylonite fabric with uniform top-to-the-SE kinematics of flow in a heterogeneous suite of rock types, ranging from feldspar porphyroclast-rich orthogneisses to garnet-bearing migmatites (Figure 8). The character and consistent direction of subhorizontal flow, combined with thermobarometric estimates, are consistent with detachment-style flow above the crust-mantle boundary [*Tikoff et al.*, 2002; *Weber*, 1986; *Williams and Jiang*, 2005]. The record of relatively low-viscosity subhorizontal shear strain at ~30 km depths implies that stresses were horizontally transmitted through the crust as it was decoupled from the underlying crust/mantle [*Royden*, 1996]. Stretching and striping lineations associated with recumbent isoclinal folds of compositional layering qualitatively attest to dramatic transposition of material and a component of subvertical thickening during lower crustal flow (Figures 6d, 7, and 9) [e.g., *Sengupta and Ghosh*, 2007]. Subhorizontal fabric development and $L \gg S$ to L-tectonite strain in the banded gneisses was overprinted by upright meter-scale corrugations coaxial with L_1 (domain 3, Figures 5a, 5b, and 5f). Lower crustal flow during D_1 was thus affected by a component of y axis shortening in the waning stages of constrictional strain [e.g., *Mancktelow and Pavlis*, 1994]. The production of penetrative subhorizontal fabrics, corrugations, and L-tectonites is attributed to heterogeneous D_1 lower crustal flow.

[47] Syndeformational reactions were important during lower crustal flow, and may have facilitated further weakening and strain localization [e.g., *Rutter and Brodie*, 1995; *Stünitz and Tullis*, 2001]. Metamorphic reactions were synkinematic in the orthogneisses, with preferential nucleation of high-Ca garnet and amphibole in the Na-rich mantles of recrystallized plagioclase porphyroclasts during top-to-the-SE subhorizontal shear strain (Figures 12 and 13).

Synkinematic growth of garnet at the expense of dynamically recrystallized plagioclase is attributed to isobaric cooling ± reheating during lower crustal deformation of the Mary batholith [*Williams et al.*, 2000]. The interlayered felsic granulites, in contrast to the orthogneisses, preserve a record of prograde synkinematic garnet growth, fluid-absent melting of biotite [e.g., *Vielzeuf and Montel*, 1994], and "melt weakening" [e.g., *Beaumont et al.*, 2004] in the waning stages of batholith emplacement.

[48] The layered subhorizontal S_1 tectonite fabric exposed along the transect is noteworthy for the general absence of grain size coarsening or pervasive annealing. Fine-grained microstructures are well preserved despite the high temperature of metamorphism and deformation (~800°C) (Figure 12). Grain sizes approach <10 μm for K-feldspar and 10–80 μm for plagioclase. These grain sizes are consistent with diffusion creep and/or grain-size-sensitive creep during lower crustal flow at relatively low viscosities (e.g., 10^{19}–10^{20} Pa s or less for nominally water-saturated plagioclase aggregates) [*Bürgmann and Dresen*, 2008; *Rybacki et al.*, 2006]. Relatively H_2O-poor and/or CO_2-rich conditions are necessary for preservation of the high-strain (i.e., fine-grained) microstructures and prevention of significant coarsening or annealing in the banded, ultramylonitic gneisses (e.g., Figures 6a, 8f, and 12) [see *Mancktelow and Pennacchioni*, 2004]. This inference is supported by estimates of 0.5 for the activity of H_2O modeled in this study for garnet + amphibole orthogneisses and by the presence of interstitial calcite throughout the Turcotte granodiorite, presumably derived from comagmatic CO_2-rich fluids.

[49] The age of S_1 fabrics, lower crustal flow, and garnet growth accompanied by partial melt production is best constrained by synkinematic, Y-depleted monazite dated at circa 2.60–2.55 Ga by EPMA in the migmatitic felsic granulites (sample 04G-067 in Figures 14, 15, and 17). Circa 2.60–2.55 Ga synkinematic monazite ages for S_1 fabrics overlap U-Pb zircon dates that are interpreted as crystallization ages for various phases of the Mary batholith at circa 2.63–2.60 Ga [*Baldwin et al.*, 2003; *Hanmer et al.*, 1994], implying a genetic link between batholith emplacement and lower crustal flow. We interpret S_1 strain as syn- to post-Mary batholith emplacement. Phases of the batholith were emplaced at depth, i.e., 0.9–1.0 GPa ≈ 30–40 km [*Williams et al.*, 2000], and thus were collectively a melt-weakened or thermally softened volume of continental lower crust capable of responding to subhorizontal flow at circa 2.60 Ga. The batholith, and the coeval Bohica mafic complex in the Northwestern domain (Figure 2), would also have provided the heat necessary to drive the partial melting and restite production represented by the felsic granulites. The tectonized, sheet-like character of many of the lithologies attests to subhorizontal strain shortly after emplacement that was enhanced during lower crustal flow (Figures 3a, 3c, 6a, and 10a). Such penetrative subhorizontal ductile fabrics provide a field-based analog for the dramatic reflectivity and anisotropy observed in the lower crust worldwide [e.g., *Meissner et al.*, 2006].

7.2. Dynamic Rheology of Continental Lower Crust: Evolution Through Time

[50] The period of Neoarchean lower crustal flow was followed by a protracted episode of isobaric cooling and lower crustal residence [*Flowers et al.*, 2008; *Mahan et al.*, 2008; *Williams et al.*, 2000; *Williams and Hanmer*, 2006]. Penetrative D_1 subhorizontal flow fabrics were overprinted by upright open to tight F_2 folds, rare axial-planar cleavage, discrete zones of steep fabric development (e.g., S_2), outcrop- to crustal-scale steeply dipping shear zones, and local reactivation and buckling of S_1 fabrics (Figure 11). The discrete and highly partitioned character of D_2 strain implies that continental lower crust, as represented by the Mary batholith, had evolved into a lower crustal "strength beam" [i.e., *Karlstrom and Williams*, 1998]. In situ EPMA monazite geochronology demonstrates that dextral shearing and NW–SE subhorizontal shortening associated with D_2 strain are Paleoproterozoic (i.e., circa 1.9 Ga in Figures 16, 17, and 18). The inferred Paleoproterozoic finite shortening direction (Figure 5h) varies from highly oblique to subparallel to the Neoarchean NW–SE trending lineations and L-tectonite strain (Figure 5f). We suggest that domains of Neoarchean L-tectonite strain were thus favorably oriented to resist penetrative reworking in the Paleoproterozoic (Figure 18). The final transect geometry (Figure 5a) represents a composite record of the effects of strain localization and strain hardening in an isobarically cooled, heterogeneous, and anisotropic sample of continental lower crust following weak lower crustal flow.

[51] Results from the Mary batholith reveal an important dichotomy that has been documented elsewhere, e.g., the lower arc crust of Fiordland [*Klepeis et al.*, 2003, 2004; 2007]. The strength of continental lower crust is dynamic and evolving. Flow of relatively weak lower crust during batholith emplacement and production of S_1 was followed by a period of near-isobaric cooling and strengthening. The character of the strengthened crust influenced subsequent deformation events. Pervasive low-viscosity flow and subhorizontal fabric development at circa 2.60–2.55 Ga contrast with the highly partitioned strain and localized shearing on steeply dipping fabrics that occurred at circa 1.9 Ga. It is noteworthy that despite the influx of heat from the mantle signaled by the Chipman mafic dike swarm at 1.896 Ga in the adjoining Chipman domain (Figure 2) [*Flowers et al.*, 2006a], the Mary batholith did not sufficiently weaken to flow or strain in the manner it did previously. Similar conclusions were drawn for the Western Fiordland Orthogneiss in New Zealand whereby zones weakened by melt and heat during lower crustal emplacement coincided with subhorizontal flow prior to cooling, strengthening, and steep fabric/shear zone development [*Klepeis et al.*, 2004].

7.3. Tectonic Implications for the Canadian Shield

[52] The circa 2.60–2.55 Ga record of Neoarchean lower crustal flow preserved in the Mary batholith temporally overlaps with S_1 fabric development and high-pressure metamorphism (1.3 GPa and 850–900°C) preserved in mafic granulites of the adjoining Chipman domain (Figure 2)

[*Flowers et al.*, 2008; *Mahan et al.*, 2008]. The timing of lower crustal flow also coincides with the period of melt and garnetiferous restite production documented in the overlying Upper Deck domain at circa 2.62–2.55 Ga (Figure 2) [*Baldwin et al.*, 2006; *Dumond et al.*, 2007]. Thus, the entire East Athabasca mylonite triangle preserves evidence for a protracted period of lower crustal flow and subhorizontal fabric development in the southeastern portion of the Athabasca granulite terrane, despite variations in lithology and age. The record of steep S_2 dextral strain identified in this study at circa 1.9 Ga overlaps in time and is kinematically compatible with slip along the adjacent crustal-scale Grease River shear zone [*Dumond et al.*, 2008]. Dextral transpression occurred throughout much of the Rae domain coincident with dextral strike-slip displacement along the Great Slave Lake and Black Bay shear zones during collision of the Churchill and Slave cratons (Figure 1a) [*Bowring et al.*, 1984; *Hanmer et al.*, 1992; *Hoffman*, 1987; *Kraus and Ashton*, 2000]. The regional occurrence of steep dextral transpressive strain is consistent with a relatively strong continental lower crust throughout much of the western Canadian Shield at circa 1.9 Ga.

[53] Neoarchean (circa 2.62–2.50 Ga) plutonism, deformation, and/or metamorphism have been identified throughout much of the western Churchill cratonic province [*Baldwin et al.*, 2006; *Flowers et al.*, 2008; *Hanmer et al.*, 1994, 2006; *MacLachlan et al.*, 2005; *Mahan et al.*, 2008; *Martel et al.*, 2008; *Mills et al.*, 2007; *Sanborn-Barrie et al.*, 2001; *Snoeyenbos et al.*, 1995; *Stern and Berman*, 2001; *Williams et al.*, 2000]. We relate the record of tectonometamorphism in the East Athabasca mylonite triangle to that preserved in the Chesterfield/Northwestern Hearne domain (Figures 1 and 2) [*Davis et al.*, 2006; *Hanmer et al.*, 2006; *MacLachlan et al.*, 2005; *Stern and Berman*, 2001]. Subhorizontal, top-the-SE lower crustal flow documented in this study may correlate with Neoarchean SE vergent thrusting observed or inferred along the Tyrell shear zone in the Yathkyed Lake supracrustal belt [*MacLachlan et al.*, 2005] and along the Big Lake shear zone that floors the Cross Bay plutonic complex further NE [*Hanmer et al.*, 2006] (Figure 1a). This correlation implies an 800 km long region of top-to-the-SE strain that is subparallel to the Snowbird tectonic zone, and may support a Neoarchean collisional origin for at least part of this >2800 km long lineament [e.g., *Jones et al.*, 2002].

8. Conclusions

[54] Subhorizontal tectonites exposed in the Mary batholith of the Athabasca granulite terrane arguably provide an important analog for the nature of lower crustal flow during orogenesis. Such analogs are critical for establishing field-based laboratories for understanding the rheology of continental lower crust [*Handy and Zingg*, 1991; *Handy et al.*, 2001; *Hodges*, 2006]. The record in this study reveals the importance of synkinematic metamorphic reactions during lower crustal flow [e.g., *Rutter and Brodie*, 1995; *Stünitz and Tullis*, 2001], in addition to the remarkable grain size reduction that attends it. Our results demonstrate the dynamic and evolving strength of continental lower crust, as observed in the roots of arcs and orogens elsewhere [e.g., *Klepeis et al.*, 2004, 2007]. In this particular case, Neoarchean subhorizontal penetrative flow of weak lower crust was followed by a period of near-isobaric cooling and strengthening. Subsequent Paleoproterozoic strain resulted in buckling and steep fabric development, discrete outcrop- to crustal-scale steeply dipping shear zones, and reactivation of S_1 gneissic fabrics. The record of strain localization and hardening recorded in the isobarically cooled Mary batholith reflects a permanently modified sample of continental lower crust that was no longer capable of weak penetrative flow. Such samples of highly anisotropic and rheologically stronger lower crust may represent "stress risers" that resist later deformation and serve to localize strain (e.g., as a lower crustal indentor or block) adjacent to weaker domains of lower or middle continental crust [e.g., *Culshaw et al.*, 2006; *Jamieson et al.*, 2007; *Klepeis et al.*, 2007].

Appendix A: Trace Element Analysis and Th-U-Pb Dating of Monazite by EPMA

[55] Thin sections were coated by vacuum thermal evaporation with ~250 Å of carbon. Monazite grains were identified by stage-scan X-ray mapping of the entire thin section at a rate of 60 ms pixel^{-1} in the Cameca® SX50 electron microprobe. Maps of raw X-ray counts for Ce$L\alpha$, P$K\alpha$, Mg$K\alpha$, and Ca$K\alpha$ (1024 × 512 pixel size) were produced utilizing a 15 kV accelerating voltage with a 350 nA beam current, a defocused beam (~30–35 μm), and a 35 μm pixel step size. High-resolution X-ray maps for individual monazite grains were collected for Y$L\alpha$, Ca$K\alpha$, Th$M\alpha$, and U$M\beta$ by stage-fixed beam rastering with a focused beam at 15 kV and 200 nA.

[56] Final thin section preparation involved removal of the C coat, followed by 4–8 h of vibratory polishing with a colloidal silica suspension. Thin sections and standards were loaded under high vacuum in a BOC Edwards Auto 306® vacuum coater, cleaned with plasma utilizing the Plasmaglo accessory, and simultaneously coated via high-precision vacuum thermal evaporation of ~200 Å Al followed by ~80 Å C.

[57] All quantitative analyses were carried out on the Cameca® SX100 "Ultrachron" electron microprobe outfitted with a LaB_6 source (Table 2). The instrument has five wavelength-dispersive spectrometers (WDS), two of which are "VL" spectrometers with very large PET crystals (2400 mm^2 in area) and detectors. The two VL spectrometers are simultaneously dedicated to analysis of Pb$M\alpha$. Count precision is increased by obtaining a weighted average of the K ratio for Pb$M\alpha$ based on the net intensities (counts per second per nanoampere) from both spectrometers [see *Jercinovic et al.*, 2008]. Combinations of natural and synthetic standards were used for calibration with a focused beam at 15 kV and 20 nA. Calibration and analysis of K$K\beta$ was carried out on the same spectrometer as U$M\beta$ to correct for the interference of K$K\alpha$ on U$M\beta$ that occurs in monazite due to X-ray fluorescence within 10–15 μm of adjacent K-bearing phases [see *Jercinovic and Williams*, 2005].

[58] Analytical points were chosen from homogeneous domains observed in high-resolution X-ray maps with emphasis placed on characterizing all observed textural/compositional variations in each monazite grain, particularly domains with distinctive microstructures. For each domain, high-resolution WDS step scans of the background spectrum around Th$M\alpha$, U$M\beta$, and Pb$M\alpha$ were collected before each set of quantitative analyses at 15 kV and 200 nA with a focused beam. Raw background scans were converted to dead time-corrected, counts per second per nanoampere and digitially filtered prior to choosing regions of the curved background spectrum that avoided interferences. The selected background regions were regressed utilizing a best fit exponential model to calculate the background intensity beneath each peak position for Th$M\alpha$, U$M\beta$, Pb$M\alpha$, and K$K\beta$ [see *Jercinovic et al.*, 2008]. Calibrated overlap correction factors for peak interferences of Y$L\gamma$ on Pb$M\alpha$, Th$M\zeta_1$ and Th$M\zeta_2$ on Pb$M\alpha$, second-order La$L\alpha$ on Pb$M\alpha$, Th$M\gamma$ on U$M\beta$, and K$K\alpha$ on U$M\beta$ were applied prior to ZAF corrections during the analytical sessions [*Donovan et al.*, 1993; *Jercinovic and Williams*, 2005; *Pyle et al.*, 2002, 2005]. Then, at least three analytical measurements were made near the background point [see *Williams et al.*, 2006]. The calibration was periodically evaluated during the analytical session by analyzing a consistency standard of known age [i.e., *Williams et al.*, 2006]. The consistency standard used in this study is the Moacyr Brazilian pegmatite Mnz with weighted mean ages of 506.4 ± 1 (2σ, MSWD = 0.56) for $^{208}Pb/^{232}Th$, 506.7 ± 0.8 Ma (2σ, MSWD = 0.83) for $^{207}Pb/^{235}U$, and 515.2 ± 0.6 Ma (2σ, MSWD = 0.36) for $^{206}Pb/^{238}U$ obtained by ID-TIMS at the Geological Survey of Canada (W. J. Davis, personal communication, 2006). Further details regarding the analytical setup and standard compositions are summarized by *Dumond et al.* [2008].

[59] **Acknowledgments.** This research was funded by NSF-EAR grants 0310004 and 0609935 to M. L. Williams and S. A. Bowring (Massachusetts Institute of Technology). Additional funding was provided by a 2005 Geological Society of America Graduate Student Research grant to G. Dumond. Field support to G. Dumond is gratefully acknowledged from the Leo Hall and Gloria Radke Memorial Funds (Department of Geosciences, University of Massachusetts). Funding for completion of this manuscript was provided by NSF EAR-PF grant 0816394 to G. Dumond. E. Gearity and N. McLean provided outstanding field assistance. Scott's General Store, Al's Place, and Transwest Airlines in Stony Rapids, Saskatchewan, are thanked for critical logistical support. Fruitful discussions on lower crustal fabric development with S. A. Bowring, R. M. Flowers, C. Kopf, K. H. Mahan, S. Phersson, N. Price, and B. Wernicke helped sharpen the ideas presented in this paper. All stereonet data presented in this contribution were produced with R. Holcombe's GEOrient© and GEOCalculator© software and R. Allmendinger's Stereonet© software.

References

Ansdell, K. M. (2005), Tectonic evolution of the Manitoba-Saskatchewan segment of the Paleoproterozoic Trans-Hudson Orogen, Canada, *Can. J. Earth Sci.*, *42*(4), 741–759, doi:10.1139/e05-035.

Ansdell, K. M., S. B. Lucas, K. Connors, and R. A. Stern (1995), Kisseynew meta-sedimentary gneiss belt, Trans-Hudson orogen (Canada): Back-arc origin and collisional inversion, *Geology*, *23*, 1039–1043, doi:10.1130/0091-7613(1995)023<1039:KMGBTH>2.3.CO;2.

Ashton, K. E., B. Knox, K. M. Bethune, and J. Marcotte (2006), Bedrock geology along the northern margin of the Athabasca Basin west of Fond-du-Lac (NTS 74O-5 and -6), south-central Beaverlodge Domain, Rae province, Fond-du-Lac Project, in *Summary of Investigations*, *Misc. Rep. 2006-4.2*, 19 pp., Sask. Geol. Surv., Sask. Ind. and Resour., Regina.

Ashton, K. E., B. Knox, and N. Rayner (2007), Geochronological update and basement geology along the northern margin of the Athabasca Basin east of Fond-du-Lac, southeastern Beaverlodge, and southwestern Tantato domains, Rae province, report, 25 pp., Sask. Geol. Surv., Sask. Ind. and Resour., Regina.

Axen, G. J., J. Selverstone, T. Byrne, and J. Fletcher (1998), If the strong crust leads, will the weak crust follow?, *GSA Today*, *8*(12), 1–7.

Baldwin, J. A., S. A. Bowring, and M. L. Williams (2003), Petrological and geochronological constraints on high pressure, high temperature metamorphism in the Snowbird tectonic zone, Canada, *J. Metamorph. Geol.*, *21*(1), 81–98, doi:10.1046/j.1525-1314.2003.00413.x.

Baldwin, J. A., S. A. Bowring, M. L. Williams, and I. S. Williams (2004), Eclogites of the Snowbird tectonic zone: Petrological and U-Pb geochronological evidence for Paleoproterozoic high-pressure metamorphism in the western Canadian Shield, *Contrib. Mineral. Petrol.*, *147*(5), 528–548, doi:10.1007/s00410-004-0572-4.

Baldwin, J. A., S. A. Bowring, M. L. Williams, and K. H. Mahan (2006), Geochronological constraints on the evolution of high-pressure felsic granulites from an integrated electron microprobe and ID-TIMS geochemical study, *Lithos*, *88*(1–4), 173–200, doi:10.1016/j.lithos.2005.08.009.

Baldwin, J. A., R. Powell, M. L. Williams, and P. Goncalves (2007), Formation of eclogite, and reaction during exhumation to mid-crustal levels, Snowbird tectonic zone, western Canadian Shield, *J. Metamorph. Geol.*, *25*(9), 953–974, doi:10.1111/j.1525-1314.2007.00737.x.

Beaumont, C., R. A. Jamieson, M. H. Nguyen, and S. Medvedev (2004), Crustal channel flows: 1. Numerical models with applications to the tectonics of the Himalayan-Tibetan orogen, *J. Geophys. Res.*, *109*, B06406, doi:10.1029/2003JB002809.

Berman, R. G., W. J. Davis, and S. Pehrsson (2007), Collisional Snowbird tectonic zone resurrected: Growth of Laurentia during the 1.9 Ga accretionary phase of the Hudsonian orogeny, *Geology*, *35*(10), 911–914, doi:10.1130/G23771A.1.

Bird, P. (1991), Lateral extrusion of lower crust from under high topography, in the isostatic limit, *J. Geophys. Res.*, *96*(B6), 10,275–10,286, doi:10.1029/91JB00370.

Bowring, S. A., W. R. Van Schmus, and P. F. Hoffman (1984), U-Pb zircon ages from Athapuscow aulacogen, East Arm of Great Slave Lake, N.W.T., Canada, *Can. J. Earth Sci.*, *21*, 1315–1324, doi:10.1139/e84-136.

Bürgmann, R., and G. Dresen (2008), Rheology of the lower crust and upper mantle: Evidence from rock mechanics, geodesy, and field observations, *Annu. Rev. Earth Planet. Sci.*, *36*, 531–567, doi:10.1146/annurev.earth.36.031207.124326.

Burov, E. B., and A. B. Watts (2006), The long-term strength of continental lithosphere: "Jelly sandwich" or "crème brûlée"?, *GSA Today*, *16*(1), 4–10, doi:10.1130/1052-5173(2006)016<4:TLTSOC>2.0.CO;2.

Butler, R. (2006), Continental lithosphere—Jelly sandwich or crème brûlée?, *Geoscientist*, *16*(8), 4–13.

Card, C. D. (2001), Basement rocks to the western Athabasca basin in Saskatchewan, in *Summary of Investigations*, *Misc. Rep. 01-4.2*, pp. 321–333, Sask. Geol. Surv., Sask. Ind. and Resour., Regina.

Corrigan, D., Z. Hajnal, B. Németh, and S. B. Lucas (2005), Tectonic framework of a Paleoproterozoic arc-continent to continent-continent collisional zone, Trans-Hudson Orogen, from geological and seismic reflection studies, *Can. J. Earth Sci.*, *42*, 421–434, doi:10.1139/e05-025.

Culshaw, N. G., R. A. Jamieson, J. W. F. Ketchum, N. Wodicka, D. Corrigan, and P. H. Reynolds (1997), Transect across the northwestern Grenville orogen, Georgian Bay, Ontario: Polystage convergence and extension in the lower orogenic crust, *Tectonics*, *16*(6), 966–982, doi:10.1029/97TC02285.

Culshaw, N. G., C. Beaumont, and R. A. Jamieson (2006), The orogenic superstructure-infrastructure concept: Revisited, quantified, and revived, *Geology*, *34*(9), 733–736, doi:10.1130/G22793.1.

Dale, J., T. Holland, and R. Powell (2000), Hornblende-garnet-plagioclase thermobarometry: A natural assemblage calibration of the thermodynamics of hornblende, *Contrib. Mineral. Petrol.*, *140*(3), 353–362, doi:10.1007/s004100000187.

Davis, W. J., S. Hanmer, S. Tella, H. A. Sandeman and J. J. Ryan (2006), U-Pb geochronology of the MacQuoid supracrustal belt and Cross Bay plutonic complex: Key components of the northwestern Hearne subdomain, western Churchill Province, Nunavut, Canada, *Precambrian Res.*, *145*(1–2), 53–80, doi:10.1016/j.precamres.2005.11.016.

Donovan, J. J., D. A. Snyder, and M. L. Rivers (1993), An improved interference correction for trace element analysis, *Microbeam Anal.*, *2*, 23–28.

Dumond, G., M. L. Williams, K. H. Mahan, M. J. Jercinovic, and R. M. Flowers (2007), Tracking the petrogenetic and rheological evolution of continental lower crust through time with monazite, *Eos Trans. AGU*, *88*(52), Fall Meet. Suppl., Abstract V34C-08.

Dumond, G., N. McLean, M. L. Williams, M. J. Jercinovic, and S. A. Bowring (2008), High-resolution dating of granite petrogenesis and deformation in a lower crustal shear zone: Athabasca granulite terrane, western Canadian Shield, *Chem. Geol.*, *254*(3–4), 175–196, doi:10.1016/j.chemgeo.2008.04.014.

Fletcher, J. M., and J. M. Bartley (1994), Constrictional strain in a noncoaxial shear zone - implications for fold and rock fabric development, central Mojave metamorphic core complex, California, *J. Struct. Geol.*, *16*(4), 555–570, doi:10.1016/0191-8141(94)90097-3.

Flowers, R., S. A. Bowring, and M. L. Williams (2006a), Timescales and significance of high-pressure, high-temperature metamorphism and mafic dike anatexis, Snowbird tectonic zone, Canada, *Contrib. Mineral. Petrol.*, *151*(5), 558–581, doi:10.1007/s00410-006-0066-7.

Flowers, R. M., K. H. Mahan, S. A. Bowring, M. L. Williams, M. S. Pringle, and K. V. Hodges (2006b), Multistage exhumation and juxtaposition of lower continental crust in the western Canadian Shield: Linking high-resolution U-Pb and $^{40}Ar/^{39}Ar$ thermochronometry with pressure-temperature-deformation paths, *Tectonics*, *25*, TC4003, doi:10.1029/2005TC001912.

Flowers, R. M., S. A. Bowring, K. H. Mahan, M. L. Williams, and I. S. Williams (2008), Stabilization and reactivation of cratonic lithosphere from the lower crustal record in the western Canadian shield, *Contrib. Mineral. Petrol.*, *156*(4), 529–549, doi:10.1007/s00410-008-0301-5.

Foster, G., H. D. Gibson, R. Parrish, M. Horstwood, J. Fraser, and A. Tindle (2002), Textural, chemical and isotopic insights into the nature and behaviour of metamorphic monazite, *Chem. Geol.*, *191*(1–3), 183–207, doi:10.1016/S0009-2541(02)00156-0.

Foster, G., R. R. Parrish, M. S. A. Horstwood, S. Chenery, J. Pylee, and H. D. Gibson (2004), The generation of prograde P-T-t points and paths; a textural, compositional, and chronological study of metamorphic monazite, *Earth Planet. Sci. Lett.*, *228*(1–2), 125–142, doi:10.1016/j.epsl.2004.09.024.

Gibson, H. D., S. D. Carr, R. L. Brown, and M. A. Hamilton (2004), Correlations between chemical and age domains in monazite, and metamorphic reactions involving major pelitic phases: An integration of ID-TIMS and SHRIMP geochronology with Y-Th-U X-ray mapping, *Chem. Geol.*, *211*(3–4), 237–260, doi:10.1016/j.chemgeo.2004.06.028.

Gilboy, C. F. (1980), Bedrock compilation geology: Stony Rapids area (NTS 74P)—Preliminary geological map, scale 1:250,000, Sask. Geol. Surv., Sask. Energy and Mines, Regina.

Gratton, J. (1989), Crustal shortening, root spreading, isostasy, and the growth of orogenic belts: A dimensional analysis, *J. Geophys. Res.*, *94*(B11), 15,627–15,634, doi:10.1029/JB094iB11p15627.

Green, D. H., and A. E. Ringwood (1967), An experimental investigation of the gabbro to eclogite transformation and its petrological applications, *Geochim. Cosmochim. Acta*, *31*, 767–833, doi:10.1016/S0016-7037(67)80031-0.

Hacker, B. R., and P. B. Gans (2005), Continental collisions and the creation of ultrahigh-pressure terranes: Petrology and thermochronology of nappes in the central Scandinavian Caledonides, *Geol. Soc. Am. Bull.*, *117*(1–2), 117–134, doi:10.1130/B25549.1.

Haines, S. S., S. L. Klemperer, L. Brown, J. Guo, J. Mechie, R. Meissner, A. Ross, and W. Zhao (2003), INDEPTH III seismic data: From surface observations to deep crustal processes in Tibet, *Tectonics*, *22*(1), 1001, doi:10.1029/2001TC001305.

Hajnal, Z., J. Lewry, D. White, K. Ashton, R. Clowes, M. Stauffer, I. Gyorfi, and E. Takacs (2005), The Sask Craton and Hearne Province margin: Seismic reflection studies in the western Trans-Hudson Orogen, *Can. J. Earth Sci.*, *42*(4), 403–419, doi:10.1139/e05-026.

Handy, M. R., and A. Zingg (1991), The tectonic and rheological evolution of an attenuated cross-section of the continental crust: Ivrea crustal section, southern Alps, northwestern Italy and southern Switzerland, *Geol. Soc. Am. Bull.*, *103*(2), 236–253, doi:10.1130/0016-7606(1991)103<0236:TTAREO>2.3.CO;2.

Handy, M. R., J. Braun, M. Brown, N. Kukowski, M. S. Paterson, S. M. Schmid, B. Stöckhert, K. Stüwe, A. B. Thompson, and E. Wosnitza (2001), Rheology and geodynamic modelling: The next step forward, *Int. J. Earth Sci.*, *90*(1), 149–156, doi:10.1007/s005310000161.

Hanmer, S. (1994), Geology, East Athabasca mylonite triangle, Saskatchewan, *Map 1859A*, scale 1:100,000, Geol. Surv. of Can., Ottawa.

Hanmer, S. (1997), Geology of the Striding-Athabasca mylonite zone, northern Saskatchewan and southeastern District of Mackenzie, Northwest Territories, *Pap. Geol. Surv. Can.*, *93-1E*.

Hanmer, S., S. Bowring, O. van Breemen, and R. Parrish (1992), Great Slave Lake shear zone, northwest Canada: Mylonitic record of Early Proterozoic convergence, collision, and indentation, *J. Struct. Geol.*, *14*, 757–773, doi:10.1016/0191-8141(92)90039-Y.

Hanmer, S., R. Parrish, M. Williams, and C. Kopf (1994), Striding-Athabasca mylonite zone: Complex Archean deep crustal deformation in the East Athabasca mylonite triangle, N. Saskatchewan, *Can. J. Earth Sci.*, *31*, 1287–1300, doi:10.1139/e94-111.

Hanmer, S., M. Williams and C. Kopf (1995), Modest movements, spectacular fabrics in an intracontinental deep-crustal strike-slip fault: Striding-Athabasca mylonite zone, NW Canadian Shield, *J. Struct. Geol.*, *17*(4), 493–507, doi:10.1016/0191-8141(94)00070-G.

Hanmer, S., S. Tella, J. J. Ryan, H. A. Sandeman and R. G. Berman (2006), Late Neoarchean thick-skinned thrusting and Paleoproterozoic reworking in the MacQuoid supracrustal belt and cross bay plutonic complex, western Churchill Province, Nunavut, Canada, *Precambrian Res.*, *144*(1–2), 126–139, doi:10.1016/j.precamres.2005.10.005.

Hartlaub, R. P., T. Chacko, L. M. Heaman, R. A. Creaser, K. E. Ashton, and A. Simonetti (2005), Ancient (Meso- to Paleoarchean) crust in the Rae Province, Canada: Evidence from Sm-Nd and U-Pb constraints, *Precambrian Res.*, *141*, 137–153, doi:10.1016/j.precamres.2005.09.001.

Hauck, M. L., K. D. Nelson, L. D. Brown, W. Zhao, and A. R. Ross (1998), Crustal structure of the Himalayan orogen at ~90° east longitude from Project INDEPTH deep reflection profiles, *Tectonics*, *17*(4), 481–500, doi:10.1029/98TC01314.

Hodges, K. V. (2006), A synthesis of the channel flow—Extrusion hypothesis as developed for the Himalayan-Tibetan orogenic system, in *Channel Flow, Ductile Extrusion and Exhumation in Continental Collision Zones*, edited by R. D. Law et al., *Geol. Soc. Spec. Publ.*, *268*, 71–90.

Hoffman, P. F. (1987), Continental transform tectonics; Great Slave Lake shear zone (ca. 1.9 Ga), northwest Canada, *Geology*, *15*(9), 785–788, doi:10.1130/0091-7613(1987)15<785:CTTGSL>2.0.CO;2.

Hoffman, P. F. (1988), United Plates of America, the birth of a craton: Early Proterozoic assembly and growth of Laurentia, *Annu. Rev. Earth Planet. Sci.*, *16*, 543–603, doi:10.1146/annurev.ea.16.050188.002551.

Holland, T. J. B., and R. Powell (1998), An internally consistent thermodynamic data set for phases of petrological interest, *J. Metamorph. Geol.*, *16*(3), 309–343, doi:10.1111/j.1525-1314.1998.00140.x.

Jackson, J. (2002), Strength of the continental lithosphere: Time to abandon the jelly sandwich?, *GSA Today*, *12*(9), 4–10, doi:10.1130/1052-5173(2002)012<0004:SOTCLT>2.0.CO;2.

Jamieson, R. A., C. Beaumont, S. Medvedev, and M. H. Nguyen (2004), Crustal channel flows: 2. Numerical models with implications for metamorphism in the Himalayan-Tibetan orogen, *J. Geophys. Res.*, *109*, B06407, doi:10.1029/2003JB002811.

Jamieson, R. A., C. Beaumont, M. H. Nguyen, and N. G. Culshaw (2007), Synconvergent ductile flow in variable-strength continental crust: Numerical models with application to the western Grenville orogen, *Tectonics*, *26*, TC5005, doi:10.1029/2006TC002036.

Jercinovic, M. J., and M. L. Williams (2005), Analytical perils (and progress) in electron microprobe trace element analysis applied to geochronology: Background acquisition, interferences, and beam irradiation effects, *Am. Mineral.*, *90*(4), 526–546, doi:10.2138/am.2005.1422.

Jercinovic, M. J., M. L. Williams, and E. D. Lane (2008), In-situ trace element analysis of monazite and other fine-grained accessory minerals by EPMA, *Chem. Geol.*, *254*(3–4), 197–215, doi:10.1016/j.chemgeo.2008.05.016.

Jessell, M. W. (1987), Grain-boundary migration microstructures in a naturally deformed quartzite, *J. Struct. Geol.*, *9*, 1007–1014, doi:10.1016/0191-8141(87)90008-3.

Johnston, F. J. (1963), The Geology of the Lytle Lake Area (West Half), Saskatchewan, *SIR Rep. 80*, 20 pp., Sask. Dep. of Miner. Resour., Regina.

Jones, A. G., D. Snyder, S. Hanmer, I. Asudeh, D. White, D. Eaton, and G. Clarke (2002), Magnetotelluric and teleseismic study across the Snowbird Tectonic Zone, Canadian Shield: A Neoarchean mantle suture?, *Geophys. Res. Lett.*, *29*(17), 1829, doi:10.1029/2002GL015359.

Karlstrom, K. E., and M. L. Williams (1998), Heterogeneity of the middle crust: Implications for strength of continental lithosphere, *Geology*, *26*(9), 815–818, doi:10.1130/0091-7613(1998)026<0815:HOTMCI>2.3.CO;2.

Kelly, N. M., G. L. Clarke, and S. L. Harley (2006), Monazite behaviour and age significance in poly metamorphic high-grade terrains: A case study from the western Musgrave Block, central Australia, *Lithos*, *88*(1–4), 100–134, doi:10.1016/j.lithos.2005.08.007.

Klemperer, S. (2006), Crustal flow in Tibet: Geophysical evidence for the physical state of Tibetan lithosphere, and inferred patterns of active flow, in *Channel Flow, Ductile Extrusion and Exhumation in Continental Collision Zones*, edited by R. D. Law et al., *Geol. Soc. Spec. Publ.*, *268*, 39–70.

Klepeis, K. A., G. L. Clarke, and T. Rushmer (2003), Magma transport and coupling between deformation and magmatism in the continental lithosphere, *GSA Today*, *13*(1), 4–11, doi:10.1130/1052-5173(2003)013<0004:MTACBD>2.0.CO;2.

Klepeis, K. A., G. L. Clarke, G. Gehrels, and J. Vervoort (2004), Processes controlling vertical coupling and decoupling between the upper and lower crust of orogens: Results from Fiordland, New Zealand, *J. Struct. Geol.*, *26*(4), 765–791, doi:10.1016/j.jsg.2003.08.012.

Klepeis, K. A., D. King, M. De Paoli, G. L. Clarke, and G. Gehrels (2007), Interaction of strong lower and weak middle crust during lithospheric extension in western New Zealand, *Tectonics*, *26*, TC4017, doi:10.1029/2006TC002003.

Kohn, M. J., M. S. Wieland, C. D. Parkinson, and B. N. Upreti (2005), Five generations of monazite in Langtang gneisses: Implications for chronology of the Himalayan metamorphic core, *J. Metamorph. Geol.*, *23*(5), 399–406, doi:10.1111/j.1525-1314.2005.00584.x.

Kopf, C. F. (1999), Deformation, metamorphism, and magmatism in the East Athabasca Mylonite Triangle, northern Saskatchewan: Implications for the Archean and Early Proterozoic crustal structure of the Canadian Shield, 156 pp., Ph.D. thesis, Univ. of Mass., Amherst.

Kraus, J., and K. E. Ashton (2000), New insights into the structural geology and tectonic setting of the

Uranium City area, northwestern Saskatchewan, in *Summary of Investigations*, *Misc. Rep. 01-4.2*, pp. 16–25, Sask. Geol. Surv., Sask. Ind. and Resour., Regina.

Krikorian, L. (2002), Geology of the Wholdaia Lake segment of the Snowbird Tectonic Zone, Northwest Territories (Nunavut): A view of the deep crust during assembly and stabilization of the Laurentian craton, M.S. thesis, 90 pp., Univ. of Mass., Amherst.

Kruse, S., M. McNutt, J. Phipps-Morgan, L. Royden, and B. Wernicke (1991), Lithospheric extension near Lake Mead, Nevada: A model for ductile flow in the lower crust, *J. Geophys. Res.*, *96*(B3), 4435–4456, doi:10.1029/90JB02621.

Kusznir, N. J., and R. G. Park (1986), Continental lithosphere strength: The critical role of lower crustal deformation, in *The Nature of the Lower Continental Crust*, edited by J. B. Dawson et al., *Geol. Soc. Spec. Publ.*, *24*, 79–93.

Leake, B. E., et al. (2003), Nomenclature of amphiboles: Additions and revisions to the International Mineralogical Association's 1997 recommendations, *Can. Mineral.*, *41*, 1355–1362, doi:10.2113/gscanmin.41.6.1355.

Macdonald, R. (1980), New edition of the geological map of Saskatchewan, Precambrian Shield area, in *Summary of Investigations*, *Misc. Rep. 01-4.2*, pp. 19–21, Sask. Geol. Surv., Sask. Ind. and Resour., Regina.

MacLachlan, K., W. J. Davis, and C. Relf (2005), U/Pb geochronological constraints on Neoarchean tectonism: Multiple compressional events in the northwestern Hearne Domain, Western Churchill Province, Canada, *Can. J. Earth Sci.*, *42*(1), 85–109, doi:10.1139/e04-104.

Mahan, K. H., and M. L. Williams (2005), Reconstruction of a large deep-crustal terrane: Implications for the Snowbird tectonic zone and early growth of Laurentia, *Geology*, *33*(5), 385–388, doi:10.1130/G21273.1.

Mahan, K. H., M. L. Williams, and J. A. Baldwin (2003), Contractional uplift of deep crustal rocks along the Legs Lake shear zone, western Churchill Province, Canadian Shield, Can. *J. Earth Sci.*, *40*(8), 1085–1110, doi:10.1139/e03-039.

Mahan, K. H., P. Goncalves, M. L. Williams, and M. J. Jercinovic (2006a), Dating metamorphic reactions and fluid flow: Application to exhumation of high- P granulites in a crustal-scale shear zone, western Canadian Shield, *J. Metamorph. Geol.*, *24*(3), 193–217, doi:10.1111/j.1525-1314.2006.00633.x.

Mahan, K. H., M. L. Williams, R. M. Flowers, M. J. Jercinovic, J. A. Baldwin, and S. A. Bowring (2006b), Geochronological constraints on the Legs Lake shear zone with implications for regional exhumation of lower continental crust, western Churchill Province, Canadian Shield, *Contrib. Mineral. Petrol.*, *152*(2), 223–242, doi:10.1007/s00410-006-0106-3.

Mahan, K. H., P. Goncalves, R. Flowers, M. L. Williams, and D. Hoffman-Setka (2008), The role of heterogeneous strain in the development and preservation of a polymetamorphic record in high-P granulites, western Canadian Shield, *J. Metamorph. Geol.*, *26*(6), 669–694, doi:10.1111/j.1525-1314.2008.00783.x.

Mancktelow, N. S., and T. L. Pavlis (1994), Fold-fault relationships in low-angle detachment systems, *Tectonics*, *13*(3), 668–685, doi:10.1029/93TC03489.

Mancktelow, N. S., and G. Pennacchioni (2004), The influence of grain boundary fluids on the microstructure of quartz-feldspar mylonites, *J. Struct. Geol.*, *26*(1), 47–69, doi:10.1016/S0191-8141(03)00081-6.

Martel, E., and K. Pierce (2006), An ArcView 3.x digital geological atlas of the Snowbird Lake area, *NTS 65D, NWT Open File 2006-02*, Northwest Territories Geosci. Off., Yellowknife, Canada.

Martel, E., O. van Breemen, R. G. Berman, and S. Pehrsson (2008), Geochronology and tectonometamorphic history of the Snowbird Lake area, Northwest Territories, Canada: New insights into the architecture and significance of the Snowbird tectonic zone, *Precambrian Res.*, *161*(3–4), 201–230, doi:10.1016/j.precamres.2007.07.007.

McDonough, W. F., and S. S. Sun (1995), The composition of the Earth, *Chem. Geol.*, *120*(3–4), 223–253, doi:10.1016/0009-2541(94)00140-4.

Meissner, R., W. Rabbel, and H. Kern (2006), Seismic lamination and anisotropy of the lower continental crust, *Tectonophysics*, *416*(1–4), 81–99, doi:10.1016/j.tecto.2005.11.013.

Mills, A. J., R. G. Berman, W. J. Davis, S. Tella, S. Carr, C. Roddick, and S. Hanmer (2007), Thermobarometry and geochronology of the Uvauk complex, a polymetamorphic Neoarchean and Paleoproterozoic segment of the Snowbird tectonic zone, Nunavut, Canada, *Can. J. Earth Sci.*, *44*(2), 245–266, doi:10.1139/E06-080.

Nelson, K. D. (1991), Deep seismic profiling and continental evolution, in *Continental Lithosphere: Deep Seismic Reflections*, *Geodyn. Ser.*, vol. 22, edited by R. Meissner et al., pp. 377–382, AGU, Washington, D. C.

Ozacar, A. A., and G. Zandt (2004), Crustal seismic anisotropy in central Tibet: Implications for deformational style and flow in the crust, *Geophys. Res. Lett.*, *31*, L23601, doi:10.1029/2004GL021096.

Park, R. G. (1981), Origin of horizontal structure in high-grade Archean terrains, in *Archean Geology: Second International Symposium, Perth, 1980*, edited by J. E. Glover and D. I. Groves, *Spec. Publ. Geol. Soc. Aust.*, *7*, 481–490.

Passchier, C. W., and R. A. J. Trouw (2005), *Microtectonics*, 2nd ed., 366 pp., Springer, Berlin.

Percival, J. A. (1992), Exposed crustal cross sections as windows on the lower crust, in *Continental Lower Crust*, edited by D. M. Fountain et al., pp. 317–362, Elsevier, Amsterdam.

Percival, J. A., and G. F. West (1994), The Kapuskasing uplift: A geological and geophysical synthesis, *Can. J. Earth Sci.*, *31*, 1256–1286.

Powell, R., and T. Holland (1994), Optimal geothermometry and geobarometry, *Am. Mineral.*, *79*(1–2), 120–133.

Pyle, J. M., and F. S. Spear (2003), Four generations of accessory-phase growth in low-pressure migmatites from SW New Hampshire, *Am. Mineral.*, *88*, 338–351.

Pyle, J. M., F. S. Spear, R. L. Rudnick, and W. F. McDonough (2001), Monazite-xenotime-garnet equilibrium in metapelites and a new monazite-garnet thermometer, *J. Petrol.*, *42*(11), 2083–2107, doi:10.1093/petrology/42.11.2083.

Pyle, J. M., F. S. Spear and D. A. Wark (2002), Electron microprobe analysis of REE in apatite, monazite, and xenotime: Protocols and pitfalls, in *Phosphates: Geochemical, Geobiological, and Materials Importance*, *Rev. Mineral. Geochem.*, vol. 48, edited by M. J. Kohn, J. Rakovan, and J. M. Hughes, pp. 337–362, doi:10.2138/rmg.2002.48.8, Mineral. Soc. of Am., Washington, D. C.

Pyle, J. M., F. S. Spear, D. A. Wark, C. G. Daniel, and L. C. Storm (2005), Contributions to precision and accuracy of chemical ages of monazite, *Am. Mineral.*, *90*, 547–577, doi:10.2138/am.2005.1340.

Rainbird, R. H., et al. (2007), Age, provenance, and regional correlation of the Athabasca Group, Saskatchewan and Alberta, constrained by igneous and detrital zircon geochronology, in *EXTECH IV: Geology and Uranium EXploration TECHnology of the Proterozoic Athabasca Basin, Saskatchewan and Alberta*, edited by C. W. Jefferson and G. Delaney, *Bull. Geol. Surv. Can.*, *588*, 193–209.

Ramsay, J. G. (1967), *Folding and Fracturing of Rocks*, 2nd ed., Blackburn, Caldwell, N. J.

Ramsay, J. G., and M. I. Huber (1983), *Strain Analysis*, 307 pp., Academic, London.

Ramsay, J. G., and M. I. Huber (1987), *Folds and Fractures*, 700 pp., Academic, London.

Ross, A. R., L. D. Brown, P. Pananont, K. D. Nelson, S. Klemperer, S. Haines, W. Zhao, and J. Guo (2004), Deep reflection surveying in central Tibet: Lower-crustal layering and crustal flow, *Geophys. J. Int.*, *156*(1), 115–128, doi:10.1111/j.1365-246X.2004.02119.x.

Ross, G. M. (2002), Evolution of Precambrian continental lithosphere in western Canada: Results from Lithoprobe studies in Alberta and beyond, *Can. J. Earth Sci.*, *39*(3), 413–437, doi:10.1139/e02-012.

Roure, F., P. Choukroune, X. Berastegui, J. A. Munoz, A. Villien, P. Matheron, M. Bareyt, M. Seguret, P. Camara, and J. Deramond (1989), ECORS deep seismic data and balanced cross sections: Geometric constraints on the evolution of the Pyrenees, *Tectonics*, *8*(1), 41–50, doi:10.1029/TC008i001p00041.

Royden, L. (1996), Coupling and decoupling of crust and mantle in convergent orogens: Implications for strain partitioning in the crust, *J. Geophys. Res.*, *101*(B8), 17,679–17,705, doi:10.1029/96JB00951.

Royden, L. H., B. C. Burchfiel, R. W. King, E. Wang, Z. Chen, F. Shen, and Y. Liu (1997), Surface deformation and lower crustal flow in eastern Tibet, *Science*, *276*(5313), 788–790, doi:10.1126/science.276.5313.788.

Royden, L. H., et al. (2008), The geological evolution of the Tibetan plateau, *Science*, *321*, 1054–1058, doi:10.1126/science.1155371.

Rutter, E. H., and K. H. Brodie (1992), Rheology of the lower crust, in *Continental Lower Crust*, edited by D. M. Fountain et al., pp. 201–267, Elsevier, Amsterdam.

Rutter, E. H., and K. H. Brodie (1995), Mechanistic interactions between deformation and metamorphism, *Geol. J.*, *30*(3–4), 227–240, doi:10.1002/gj.3350300304.

Rybacki, E., M. Gottschalk, R. Wirth, and G. Dresen (2006), Influence of water fugacity and activation volume on the flow properties of fine-grained anorthite aggregates, *J. Geophys. Res.*, *111*, B03203, doi:10.1029/2005JB003663.

Sanborn-Barrie, M., S. Carr, and R. Thériault (2001), Geochronological constraints on metamorphism, magmatism and exhumation of deep-crustal rocks of the Kramanituar Complex, with implications for the Paleoproterozoic evolution of the Archean western Churchill Province, Canada, *Contrib. Mineral. Petrol.*, *141*, 592–612, doi:10.1007/s004100100262.

Sandiford, M. (1989), Horizontal structures in granulite terrains: A record of mountain building or mountain collapse, *Geology*, *17*, 449–452, doi:10.1130/0091-7613(1989)017<0449:HSIGTA>2.3.CO;2.

Sandiford, M., and R. Powell (1986), Deep crustal metamorphism during continental extension: Modern and ancient examples, *Earth Planet. Sci. Lett.*, *79*, 151–158, doi:10.1016/0012-821X(86)90048-8.

Sengupta, S., and S. K. Ghosh (2007), Origin of striping lineation and transposition of linear structures in shear zones, *J. Struct. Geol.*, *29*(2), 273–287, doi:10.1016/j.jsg.2006.08.012.

Slimmon, W. L. (1989), Bedrock compilation geology—Fond du Lac (NTS 74-O), *Map 247A*, scale 1:250,000, Sask. Geol. Surv., Sask. Energy and Mines, Regina.

Snoeyenbos, D. R., M. L. Williams, and S. Hanmer (1995), Archean high-pressure metamorphism in the western Canadian Shield, *Eur. J. Mineral.*, *7*, 1251–1272.

Stern, R. A., and R. G. Berman (2001), Monazite U-Pb and Th-Pb geochronology by ion microprobe, with an application to in situ dating of an Archean metasedimentary rock, *Chem. Geol.*, *172*(1–2), 113–130, doi:10.1016/S0009-2541(00)00239-4.

St-Onge, M. R., M. P. Searle, and N. Wodicka (2006), Trans-Hudson Orogen of North America and Himalaya-Karakoram-Tibetan Orogen of Asia: Structural and thermal characteristics of the lower and upper plates, *Tectonics*, *25*, TC4006, doi:10.1029/2005TC001907.

Stünitz, H., and J. Tullis (2001), Weakening and strain localization produced by syn-deformational reaction of plagioclase, *Int. J. Earth Sci.*, *90*(1), 136–148, doi:10.1007/s005310000148.

Tella, S., et al. (2000), 1:100000 scale bedrock geology compilation map of the MacQuoid Lake-Gibson Lake-Cross Bay-Akunak Bay region, western Churchill province, Nunavut, Canada, *Geol. Assoc. Can. Mineral. Assoc. Can. Program Abstr.*, *25*, 676.

Teyssier, C. (1985), A crustal thrust system in an intracratonic environment, *J. Struct. Geol.*, *7*, 689–700, doi:10.1016/0191-8141(85)90144-0.

Thatcher, W., and F. F. Pollitz (2008), Temporal evolution of continental lithospheric strength in actively deforming regions, *GSA Today*, *18*(4–5), 4–11, doi:10.1130/GSAT01804-5A.1.

Tikoff, B., C. Teyssier, and C. Waters (2002), Clutch tectonics and the partial attachment of lithospheric layers, in *Continental Collision and the Tectono-Sedimentary Evolution of Forelands*, edited by G. Bertotti et al., pp. 57–73, Eur. Geophys. Union, Katlenburg-Lindau, Germany.

Tullis, J. (2002), Deformation of granitic rocks: Experimental studies and natural examples, in *Plastic Deformation in Minerals and Rocks*, *Rev. Mineral. Geochem.*, vol. 51, edited by S. Karato and H.-R. Wenk, pp. 51–96, Mineral. Soc. of Am., Washington, D. C.

van Breeman, O., C. T. Harper, R. G. Berman, and N. Wodicka (2007a), Crustal evolution and Neoarchean assembly of the central-southern Hearne domains: Evidence from U-Pb geochronology and Sm-Nd isotopes of the Phelps Lake area, northeastern Saskatchewan, *Precambrian Res.*, *159*, 33–59, doi:10.1016/j.precamres.2007.04.014.

van Breeman, O., S. Pehrsson, and T. D. Peterson (2007b), Reconnaissance U-Pb SHRIMP geochronology and Sm-Nd isotope analyses from the Tehery-Wager Bay gneiss domain, western Churchill Province, *Curr. Res. Geol. Surv. Can.*, *2007–F2*, 15 pp.

Vielzeuf, D., and J. M. Montel (1994), Partial melting of metagreywackes. Part I. Fluid-absent experiments and phase relationships, *Contrib. Mineral. Petrol.*, *117*(4), 375–393, doi:10.1007/BF00307272.

Weber, K. (1986), Metamorphism and crustal rheology—Implications for the structural development of the continental crust during prograde metamorphism, in *The Nature of the Lower Continental Crust*, edited by J. B. Dawson et al., *Geol. Soc. Spec. Publ.*, *24*, 95–106.

Wernicke, B., J. L. Davis, N. A. Niemi, P. Luffi, and S. Bisnath (2008), Active megadetachment beneath the western United States, *J. Geophys. Res.*, *113*, B11409, doi:10.1029/2007JB005375.

Westaway, R. (1995), Crustal volume balance during the India-Eurasia collision and altitude of the Tibetan Plateau: A working hypothesis, *J. Geophys. Res.*, *100*(B8), 15,173–15,192, doi:10.1029/95JB01310.

Whitmeyer, S. J., and K. E. Karlstrom (2007), Tectonic model for the Proterozoic growth of North America, *Geosphere*, *3*(4), 220–259, doi:10.1130/GES00055.1.

Williams, M. L., and S. Hanmer (2006), Structural and metamorphic processes in the lower crust: Evidence from a deep-crustal isobarically cooled terrane, Canada, in *Evolution and Differentiation of the Continental Crust*, edited by M. Brown and T. Rushmer, pp. 231–267, Cambridge Univ. Press, Cambridge.

Williams, M. L., and M. J. Jercinovic (2002), Microprobe monazite geochronology: putting absolute time into microstructural analysis, *J. Struct. Geol.*, *24*, 1013–1028, doi:10.1016/S0191-8141(01)00088-8.

Williams, P. F., and D. Z. Jiang (2005), An investigation of lower crustal deformation: Evidence for channel flow and its implications for tectonics and structural studies, *J. Struct. Geol.*, *27*(8), 1486–1504, doi:10.1016/j.jsg.2005.04.002.

Williams, M. L., S. Hanmer, C. Kopf, and M. Darrach (1995), Syntectonic generation and segregation of tonalitic melts from amphibolite dikes in the lower crust, Striding-Athabasca mylonite zone, northern Saskatchewan, *J. Geophys. Res.*, *100*(B8), 15,717–15,734, doi:10.1029/95JB00760.

Williams, M. L., E. A. Melis, C. F. Kopf, and S. Hanmer (2000), Microstructural tectonometamorphic processes and the development of gneissic layering: A mechanism for metamorphic segregation, *J. Metamorph. Geol.*, *18*, 41–57, doi:10.1046/j.1525-1314.2000.00235.x.

Williams, P. F., D. Jiang, and S. Lin (2006), Interpretation of deformation fabrics of infrastructure zone rocks in the context of channel flow and other tectonic models, in *Channel Flow, Ductile Extrusion and Exhumation in Continental Collision Zones*, edited by R. D. Law et al., *Geol. Soc. Spec. Publ.*, *268,* 221–235.

Williams, M. L., M. J. Jercinovic, and C. J. Hetherington (2007), Microprobe monazite geochronology: Understanding geologic processes by integrating composition and chronology, *Annu. Rev. Earth Planet. Sci.*, *35*(1), 137–175, doi:10.1146/annurev.earth.35.031306.140228.

Wilson, C. K., C. H. Jones, P. Molnar, A. F. Sheehan, and O. S. Boyd (2004), Distributed deformation in the lower crust and upper mantle beneath a continental strike-slip fault zone: Marlborough fault system, South Island, New Zealand, *Geology*, *32*(10), 837–840, doi:10.1130/G20657.1.

Zhu, X. K., and R. K. O'Nions (1999), Monazite chemical composition: Some implications for monazite geochronology, *Contrib. Mineral. Petrol.*, *137*(4), 351–363, doi:10.1007/s004100050555.

G. Dumond, Department of Earth, Atmospheric, and Planetary Sciences, Massachusetts Institute of Technology, 77 Massachusetts Ave., 54-1126, Cambridge, MA 02139, USA. (gdumond@mit.edu)

P. Goncalves, UMR 6249 Chrono-Envrionnement, Université de Franche-Comté, 16 route de Gray, F-25030 Besançon, France.

M. J. Jercinovic and M. L. Williams, Department of Geosciences, University of Massachusetts, Amherst, MA 01003-9297, USA.